Ionospheric Conductances Derived From Electrodynamic Models

Daniel R Weimer[1] and Thom R Edwards[2]

[1]Virginia Tech
[2]DTU Space, Technical University of Denmark

November 22, 2022

Abstract

We have used empirical models for electric potentials and the magnetic fields in both space and on the ground to obtain maps of the height-integrated Pedersen and Hall ionospheric conductivities at high latitudes. This calculation required use of both "curl-free" and "divergence-free" components of the ionospheric currents, with the former obtained from magnetic fields that are used in a model of the field-aligned currents. The second component is from the equivalent current, usually associated with Hall currents, derived from the ground-level magnetic field. Conductances were calculated for varying combinations of the Interplanetary magnetic field (IMF) magnitude and orientation angle, as well as the dipole tilt angle. The results show that reversing the sign of the Y component of the IMF produces substantially different conductivity patterns. The Hall conductivities are largest on the dawn side in the upward, Region 2 field-aligned currents. Low electric field strengths in the Harang discontinuity lead to inconclusive results near midnight. Calculations of the Joule heating, obtained from the electric field and both components of the ionospheric current, are compared with the Poynting flux in space. The maps show some differences, while their integrated totals match to within 1%. Some of the Poynting flux that enters the polar cap is dissipated as Joule heating within the auroral ovals, where the conductivity is enhanced, confirming the Poynting Flux theorem proposed by Richmond in 2010, for the first time using realistic electric fields, ionospheric currents, and conductivity.

Ionospheric Conductances Derived From Electrodynamic Models

D. R. Weimer[1,2] and Thom R. Edwards[3]

[1]Center for Space Science and Engineering Research, Virginia Tech, Blacksburg, Virginia, USA
[2]National Institute of Aerospace, Hampton, Virginia, USA
[3]Danish Technical University, Copenhagen, Denmark

Key Points:

- Models of electric potentials, field-aligned current, and magnetic perturbations are used together to calculate ionospheric conductivities
- The sign of the Y component of the IMF has a strong influence on conductivity values
- Differences between the Poynting flux and Joule heating are demonstrated with realistic electric fields and ionospheric currents

Corresponding author: Daniel Weimer, `dweimer@vt.edu`

Abstract

We have used empirical models for electric potentials and the magnetic fields in both space and on the ground to obtain maps of the height-integrated Pedersen and Hall ionospheric conductivities at high latitudes. This calculation required use of both "curl-free" and "divergence-free" components of the ionospheric currents, with the former obtained from magnetic fields that are used in a model of the field-aligned currents. The second component is from the equivalent current, usually associated with Hall currents, derived from the ground-level magnetic field. Conductances were calculated for varying combinations of the Interplanetary magnetic field (IMF) magnitude and orientation angle, as well as the dipole tilt angle. The results show that reversing the sign of the Y component of the IMF produces substantially different conductivity patterns. The Hall conductivities are largest on the dawn side in the upward, Region 2 field-aligned currents. Low electric field strengths in the Harang discontinuity lead to inconclusive results near midnight. Calculations of the Joule heating, obtained from the electric field and both components of the ionospheric current, are compared with the Poynting flux in space. The maps show some differences, while their integrated totals match to within 1%. Some of the Poynting flux that enters the polar cap is dissipated as Joule heating within the auroral ovals, where the conductivity is enhanced, confirming the Poynting Flux theorem proposed by Richmond in 2010, for the first time using realistic electric fields, ionospheric currents, and conductivity.

Plain Language Summary

The conductance of the ionosphere at high latitudes is an important quantity in space science as it governs the relationship between the electric fields and currents. There are two types of conductance values, and both are difficult to measure. Variations with the level of auroral activity make exact values a challenge to determine with accuracy. This study has derived the conductance values using a combination of empirical models that produce maps of the electric and magnetic fields, both in space and on the ground, that vary according to how strong the magnetosphere is driven by the solar wind. The results show that the conductances have a dawn-dusk asymmetry that is dependent on the orientation of the magnetic field in the solar wind. The results may be useful in numerical simulations of the Earth's magnetosphere, but the values calculated in some regions are uncertain, particularly near local midnight. An unexpected outcome from this work was verification of a prior theory indicating that the distribution of the electric heating in the ionosphere could differ from the energy flow that is mapped in space with satellites, even though their total sum in the polar region is the same.

1 Introduction

The Earth's ionosphere has a major role in the flow of currents and energy within the magnetosphere, or what is also known as the "geospace environment." The currents in the ionosphere are responsible for geomagnetic effects seen at the Earth's surface, and they also have a role in the high-latitude heating of the upper atmosphere. The magnitude of these effects is determined to a large extent by the level of conductivity in the ionosphere, and as such the conductivity needs to be accurately known for reliable geospace modeling. On the other hand, it can be argued that the conductivity values are not known with a high precision, and may be the least well-quantified part of the coupled magnetosphere-ionosphere system.

This problem is not due to a lack of understanding, as the basic equations that define the conductivity values are known. On the other hand the formulas for the Pedersen (σ_P) and Hall (σ_H) conductivities are often presented in a variety of different and confusing formats, such as in the reference books by Rees (1989); Prölss and Bird (2004); Brekke (2013). These formulas can be reduced to a more simple form:

$$\sigma_P = \frac{n_e\,|e|}{B}\left[\frac{r_e}{1+r_e^2} + \sum_i C_i \frac{r_i}{1+r_i^2}\right] \tag{1}$$

$$\sigma_H = \frac{n_e\,|e|}{B}\left[\frac{1}{1+r_e^2} - \sum_i C_i \frac{1}{1+r_i^2}\right] \tag{2}$$

where n_e is the electron number density, B is the magnitude of the magnetic field, e is the fundamental constant for the charge of an electron, and C_i is the relative ion concentration for the ith ion species, that are assumed to have a total number density equal to that of the electrons. The ratio r_i is defined as:

$$r_i = \nu_{in}/\Omega_i = 1/k_i \tag{3}$$

where k_i is the "ion mobility coefficient" (Brekke, 2013), ν_{in} is the ion-neutral or electron-neutral collision frequency, and Ω_i refers to the cyclotron frequency:

$$\Omega_i = |e|\,B/m_i \tag{4}$$

The r_e ratio is obtained substituting electrons for ions in (3) and (4). The absolute value of the electron charge is used in the equations above in order to reduce sign ambiguity.

The height-integrated values of these conductivities are often used, designated with uppercase symbols Σ_P and Σ_H. Equations (1) and (2) are similar to (5) and (6) by Mallinckrodt (1985) (with a sign correction), and simplified using (3) and (4).

In order to calculate the conductivity it is necessary to know the magnetic field strength, electron temperature and number density, and ion and neutral composition and number densities of each species. At low and mid-latitudes these quantities are better known and can be obtained from a reference magnetic field model, and familiar empirical models of the ionosphere and neutral atmosphere such as the "International Reference Ionosphere" (IRI) (Bilitza, 2001) and the Mass Spectrometer and Incoherent Scatter (MSIS) model (Hedin, 1991; Picone et al., 2002).

These models require calculations within specialized programs to generate the needed quantities, so there have been a number of attempts to construct more simple empirical formulas for the conductivity. These are mainly valid for the dayside, where solar extreme ultraviolet (EUV) radiation is the main contribution to ionization. The review paper by Brekke and Moen (1993) lists 12 different formulas spanning the years 1889 to 1992. More recently conductivity formulas were provided by Richmond (1995a), Galand and Richmond (2001), and Wiltberger et al. (2004). Assimilation techniques used in the Kamide-Richmond-Matsushita (KRM) (Kamide et al., 1981) and the Assimilated Mapping of Ionospheric Electrodynamics (AMIE) (Richmond & Kamide, 1988) methods also need to use conductivities that are derived from such models. As the solar zenith angle is used in these formulas, they often produce a sharp gradient at the terminator, so Ridley et al. (2004) had added a scattering term to the solar contribution in order to produce a smoother transition over the terminator for a coupled, magnetosphere-ionosphere numerical simulation.

At high latitudes the knowledge of the basic parameters is much less than for the lower latitudes. Due to the auroral ionization and the convection of ionized plasma from the dayside to nightside it is nearly impossible to specify the state of the ionosphere and neutral atmosphere with a high level of precision. In fact, the documentation for the IRI model states that "it provides monthly averages in the non-auroral ionosphere for magnetically quiet conditions" (http://ccmc.gsfc.nasa.gov/modelweb/ionos/iri.html). On the night side the ionization due to high-energy auroral particle precipitation contributes most significantly to conductivity enhancements, and this is where there is the greatest uncertainty.

Due to the number of "known unknowns," the ionospheric conductivity in the high-latitude region remains as one of the least-well quantified parameters in geospace and the study of magnetosphere-ionosphere coupling, yet this is where the most important interactions take place. Global numerical models may estimate the conductivities using formulas that include sunlight ionization rates and ionization production rates from precipitating particles, the recombination rates, and the equilibrium densities, and empirical models and various measurements are often used. For example, Fuller-Rowell and Evans (1987) used electron energy influx and energies from National Oceanic and Atmospheric Administration (NOAA) Television Infrared Observation Satellites (TIROS) to build statistical patterns of these data. These were used in physics-based formulas in order to calculate the Pedersen and Hall conductivities as a function of altitude, as well as the hight-integrated values, which were then used to create maps ordered by an auroral activity index. An example is shown in Figure 1.

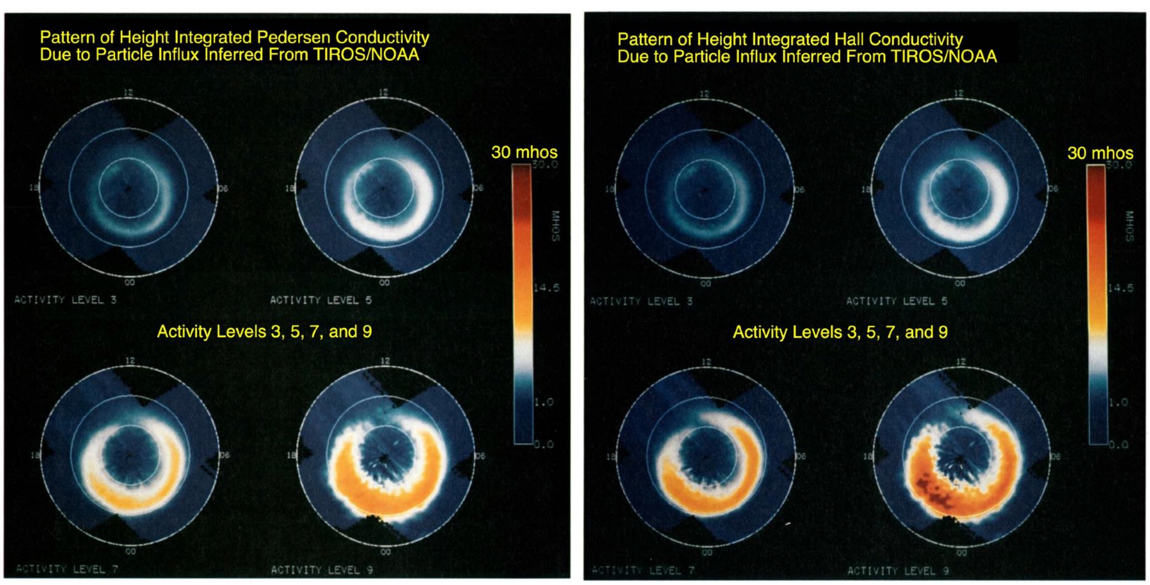

Figure 1. Example of statistical Pedersen and Hall conductivity maps derived from particle precipitations, from Plates 3 and 4 by Fuller-Rowell and Evans (1987). New text has been overlaid for clarity.

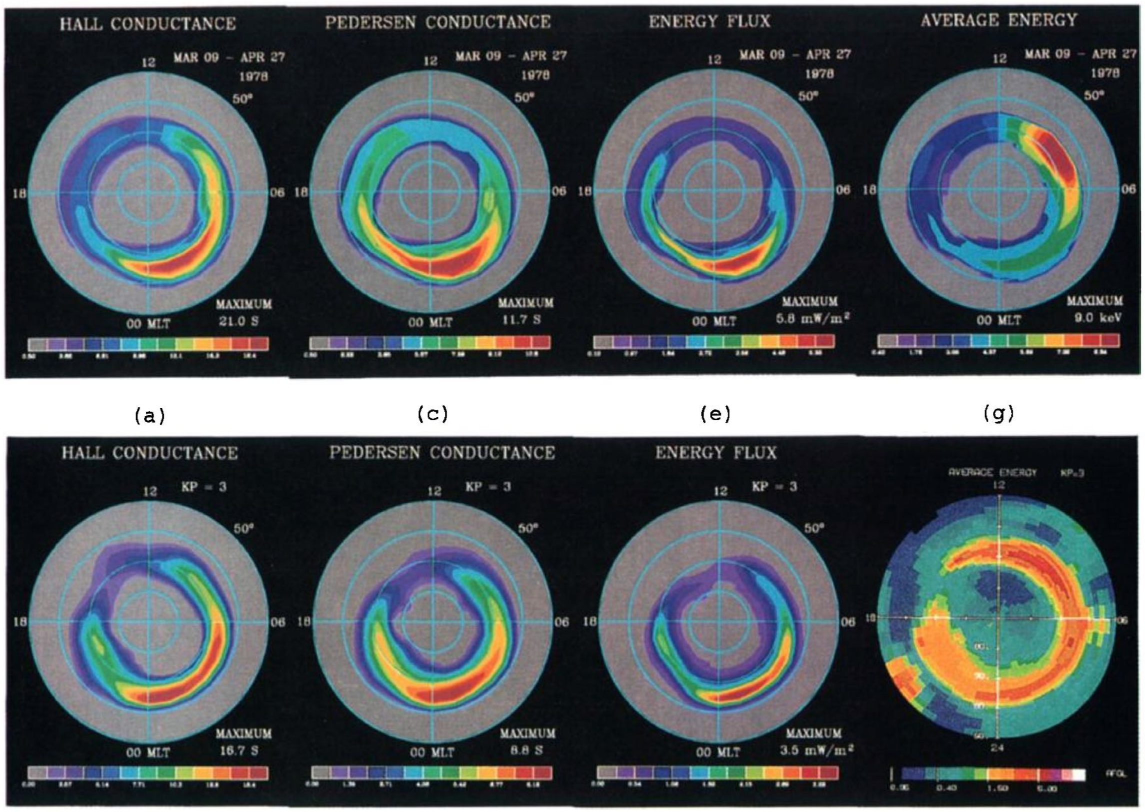

Figure 2. Comparison of results by Ahn et al. (1998) (top) with similar maps from the model by Hardy et al. (1987) (bottom), from Plate 1 by Ahn et al. (1998)

.

A similar to method was used by Hardy et al. (1987) using a statistical model of electron flux from Defense Meteorological Satellite Program (DMSP) measurements sorted by the Kp index. They had used empirical formulas derived from computations by Robinson et al. (1987), relating the conductances to the average energy and energy flux of the electrons. Ahn et al. (1998) had used radar measurements to derive conductivity, and compared these with ground observations of the magnetic perturbations in order to derive empirical relationships between them. They then used measurements of $\Delta\mathbf{B}$ to obtain global maps of the conductivity as shown in the top row of Figure 2. For comparison, the bottom row shows corresponding maps from the model by Hardy et al. (1987).

As these models don't exactly agree, the actual conductivity values are uncertain. A larger problem is that models based on activity indices have only marginal utility, as they do not take the Interplanetary Magnetic Field (IMF) vector into consideration. It is known that the electric field and field-aligned current (FAC) patterns change significantly as the IMF rotates. As it would be desirable to combine a conductivity model with an electric field or FAC model, unrealistic results are obtained if the boundaries of these models do not properly align, or if they are not from consistent IMF orientations.

There are methods for deriving conductivity maps from auroral images. For example, Lummerzheim et al. (1991) used multispectral auroral images from the Dynamics Explorer satellite to construct maps of auroral electron energy deposition and mean energy. An auroral model is used to infer conductances from brightness ratios of different spectral emissions. As this was only done for only a few individual cases the results are not actually an empirical model and there are gaps on the dayside where the auroral emissions are buried in the solar illumination, but this still a technique worth noting.

An alternative technique for obtaining the conductivity, named the "the elementary current method," (Amm, 2001) uses multiple satellite and ground magnetometer measurements for deriving the ionospheric currents. This method is based on splitting the ionospheric current vector into divergence-free ($\vec{J}_{\rm df}$) and curl-free ($\vec{J}_{\rm cf}$) parts. The total height-integrated ionospheric current that is perpendicular to the magnetic field lines is then written as:

$$\vec{J}_{\perp} = \vec{J}_{\rm df} + \vec{J}_{\rm cf} \tag{5}$$

Ground-based magnetometer data are used to derive the "divergence-free" ionospheric currents that are usually associated with Hall currents. The "curl-free" currents are derived from space-based magnetometer measurements that are sensing the field-aligned currents (FAC) that are linked to the divergence of the ionospheric currents. Thus, magnetometer measurements both above the ionosphere and on the ground are required in order to recover the full $\vec{J}_{\perp}$. More details about the derivations of these currents will follow in a later section.

From Ohm's law for the ionospheric current sheet,

$$\vec{J}_{\perp} = \Sigma_P \vec{E}_{\perp} + \Sigma_H \left(\hat{\vec{B}}_{\perp} \times \vec{E}_{\perp} \right) \tag{6}$$

if measurements of the electric field is also available then both the Pedersen and Hall conductivities can be obtained from:

$$\Sigma_P^* = \frac{\vec{J}_\perp \cdot \vec{E}_\perp}{\left|\vec{E}_\perp\right|^2} \tag{7}$$

$$\Sigma_H^* = \frac{\hat{\vec{r}} \cdot \left(\vec{J}_\perp \times \vec{E}_\perp\right)}{\left|\vec{E}_\perp\right|^2} \tag{8}$$

As Amm (2001) had stated, "These equations have been derived under the assumption that the magnetic field lines are directed perpendicular to the ionospheric plane. If they are not, the conductance tensor gets off-diagonal elements, and polarization effects have to be included." It was also noted that a small error in the direction of the vectors can produce inaccuracies, especially where the magnitude of the electric field is small. Amm (1998) indicated that the assumption that the magnetic field lines are assumed to be radial does not cause significant errors at latitudes above 45°. These formulas do not include the effects of the neutral winds on these derived values, which are assumed to be small enough to be neglected (Amm, 1995; Amm et al., 2008). We have added the * superscripts to the conductivities in (7) and (8) to indicate that these derivations are approximations, particularly due to the lack of the neutral winds, which will be covered in the Discussion section.

In the example presented by Amm (2001) the Spherical Elementary Currents Systems (SECS) (Amm, 1997; Amm & Viljanen, 1999) method is used to obtain the divergence-free currents from "the upward continuation technique for magnetic disturbance fields from the ground to the ionosphere" (Amm & Viljanen, 1999). Magnetometer measurements obtained from sites in Norway, Sweden, and Finland were used in combination with electric field values from the Scandinavian Twin Auroral Radar Experiment (STARE) coherent scatter radar. The method was demonstrated for a small area using simulated magnetic fields above the ionosphere produced by a current vortex, that were compared with measured values from an overhead pass by the four Cluster II satellites. In another example Amm et al. (2015) use the SECS methods to solve for the electric field, currents, and conductivity in the ionosphere using only measurements from two of the European Space Agency's (ESA) Swarm spacecraft. Solutions were obtained within a region spanning 7° in longitude by 20° in latitude, that bounded the parallel tracks of the two satellites.

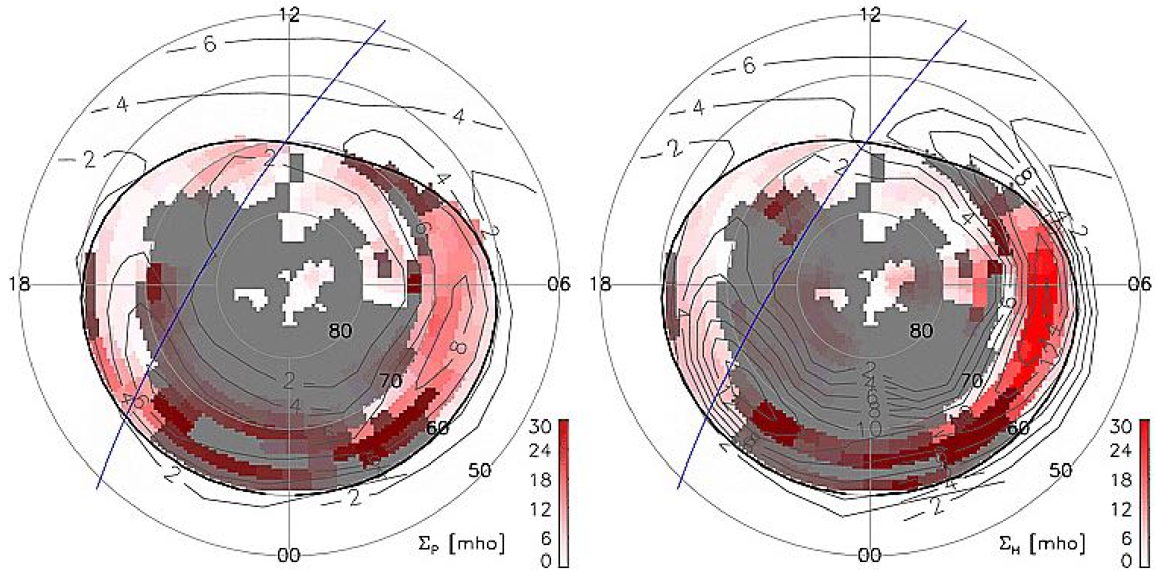

Figure 3. Pedersen (left) and Hall (right) conductivity maps, from Green et al. (2007).

The notations used in equations (6) to (8) closely follow those of Green et al. (2007), who had demonstrated their use to obtain maps of the height-integrated Pedersen and Hall conductivity over the entire polar region. The horizontal electric field in the ionosphere ($\vec{E}_\perp$) was obtained from the SuperDARN radar array, with assimilation of driftmeter, electric field measurements on the DMSP satellite along one orbit path. The SuperDARN statistical model (Ruohoniemi & Greenwald, 1996, 2005) was used to help constrain the fit of $\vec{E}_\perp$. Ground-based magnetometer data were used to construct a map of the divergence-free ionospheric current, $\vec{J}_{\rm df}$, using a Spherical Cap Harmonic Analysis (SCHA) (G. Haines, 1988) and the techniques described by Chapman and Bartels (1940) and Backus (1986). The curl-free current, $\vec{J}_{\rm cf}$, was derived from magnetic field measurements on the DMSP, Iridium, and Ørsted satellites. All data were gathered over a one-hour period while measurements by the Advanced Composition Explorer (ACE) satellite indicated that the IMF was relatively stable. The results by Green et al. (2007) are reproduced in Figure 3, with the orbit path of the DMSP 15 satellite marked with the blue line. The thick, black line marks the boundary of the fit from the SuperDARN radar data, and the grey regions indicate where there is uncertainty in the time-averaged radar measurements. The light lines show contours of the conductance from a combination of two models, by Rasmussen et al. (1988) for the solar EUV contribution and Hardy et al. (1987) for the particle precipitation contributions.

While Green et al. (2007) show results for only one event, Amm's method that they used is perhaps the most direct way to measure ionospheric conductivity. So it seems reasonable to give the technique a more thorough test. In this paper we use a similar calculation to generate more detailed maps of the conductivity for a wider range of conditions, including variations in IMF clock angle and dipole tilt angle. Our input data consist of outputs from three separate empirical models that were derived from large data sets: A new model of the electric potentials (Edwards, 2019), a model of the ground-level geomagnetic perturbations (Weimer, 2013), and a new FAC model from satellite magnetometers (Edwards et al., 2020). Due to the need for both electric fields and currents, from magnetic field measurements on both the ground and in space, we prefer to call this the "electrodynamic method."

2 Derivation of the ionospheric electric fields and currents

2.1 The electric fields

We use an updated electric potential model by Edwards (2019), which supplements the database from the Dynamics Explorer-2 spacecraft that was used by Weimer (2005b) with a substantially larger number of measurements from the Swarm spacecraft (Lomidze et al., 2019). The potential functions used in this model were fit directly from the electric field measurements, rather than first integrating the electric fields to obtain the potential prior to the fitting. This change allowed for narrowing the time window used for the associated IMF data, that provides a better temporal resolution. On all satellites only the component of the electric field in the direction of motion was usable. The electric fields in the ionosphere are the most straight-forward to obtain, calculated simply from the derivatives of the model's electric potentials. Modified magnetic apex coordinates (VanZandt et al., 1972; Richmond, 1995b) are used. This model is constructed using SCHA (G. V. Haines, 1985), with Legendre functions of real, non-integer degrees.

2.2 The divergence-free currents

The divergence-free currents are obtained from the empirical model of the ground-level magnetic fields by Weimer (2013). This model was constructed from magnetometer measurements at 149 locations during an 8-year time period, along with the simultaneous IMF measurements from the Advanced Composition Explorer (ACE) spacecraft.

All sites are located in the Northern hemisphere, extending down to the magnetic equator. Quiet-time, baseline values were subtracted from the measured magnetic fields, as described in detail by Weimer et al. (2010). These data were then translated and rotated to the magnetic apex coordinate system for use in the construction of the model. The model produces values for the Northward, Eastward, and Vertical components of the magnetic field perturbations given a specification of the Y and Z components of the IMF in Geocentric Solar Magnetic (GSM) coordinates, the solar wind velocity, dipole tilt angle, and the $F_{10.7}$ index of solar radiation.

The formulas described by Chapman and Bartels (1940), G. Haines (1988), and G. V. Haines and Torta (1994) were used to derive the “ionospheric equivalent current function” (Kamide et al., 1981; Richmond & Kamide, 1988). A detailed description of the process is provided by Weimer (2019), which includes the separation of the magnetic effects into their internal and external sources. A SCHA technique is employed, but since the size of the spherical cap is 90° the associated Legendre polynomials with integer degree are used, rather than Legendre functions of real, non-integer degrees. The end result is an expression for the external currents in terms of spherical harmonics:

$$\psi_E(\theta,\lambda) = \frac{a}{\mu_o}\sum_{k=1}^{34}\sum_{m=0}^{min(k,3)}\frac{2k+1}{k+1}\left(\frac{R_2}{a}\right)^k P_k^m(\cos\theta)(g_k^{m,e}\cos m\lambda + h_k^{m,e}\sin m\lambda) \qquad (9)$$

where R_2 is the radius of the spherical shell on which the external currents are assumed to flow, and a is the radius of the Earth. This “equivalent current” function ψ_E has units of Amperes (or kA). The current density vector is obtained from the negative gradient of this function, rotated by 90°. We use a spherical shell at an altitude of 110 km. External currents in the magnetosphere are also projected to this shell, including the ring current. As shown by Weimer (2019), better results are obtained if adjustments are made to compensate for such current. At low latitudes the Solar Quiet (Sq^o) current systems also appear in these results (Matsushita, 1975), along with the magnetic effects of inter-hemispheric, field-aligned currents, and magnetospheric currents (Yamazaki & Maute, 2017).

2.3 The curl-free currents

The new FAC model that we use was developed using a very large database of magnetic field measurements from the Ørsted, CHAMP, and Swarm missions, along with IMF values from ACE (Edwards et al., 2020). Like the previous version of the model (Weimer, 2005b), this new model is constructed using SCHA and it is based on the mathematical derivations by Backus (1986), along with Maxwell's equations. The field-aligned currents are related to the the magnetic field perturbations above the ionosphere by

$$\mu_o \mathbf{J} = \nabla \times \mathbf{\Delta B} \tag{10}$$

Following Backus (1986), the radial FAC is a poloidal current that is related to a toroidal magnetic field, such that

$$\mu_o J_{\|} \hat{\mathbf{r}} = \nabla \times (\hat{\mathbf{r}} \times \nabla_{\perp} \psi) \tag{11}$$

where ψ is a "toroidal scalar" that has units of length times magnetic induction (Tm, or more commonly used, cTm). $\nabla_{\perp}$ is a horizontal (perpendicular) surface gradient that Backus (1986) refers to as ∇_S. This last equation reduces to

$$J_{\|} = \nabla_{\perp}^2 \psi / \mu_o \tag{12}$$

As (12) can also be written as

$$J_{\|} = \nabla_{\perp} \cdot (\nabla_{\perp} \psi / \mu_o) = \nabla_{\perp} \cdot \vec{J}_{\text{cf}} \tag{13}$$

it is seen the FAC density is related to the divergence of the curl-free "potential current," where

$$\vec{J}_{\text{cf}} = \nabla_{\perp} \psi / \mu_o = -\hat{\mathbf{r}} \times \Delta \mathbf{B} / \mu_{\mathbf{o}} \tag{14}$$

and $\hat{\mathbf{r}}$ is downward in the direction of the local magnetic field. A positive field-aligned current is also downward. This result indicates that the curl-free current is in the direction of the gradient of the toroidal scalar. Additionally, this gradient is rotated 90° from the direction of the toroidal component of the magnetic field, and vice versa.

The newest model by Edwards et al. (2020) differs from the predecessors in that the magnetic potential function is not used. Instead, the two horizontal components of the magnetic field are fit directly to the values measured on the spacecraft, after subtraction of the Earth's internal field and translation into magnetic apex coordinates. The FAC is then calculated directly from (10), rather than (12), and the curl-free currents are calculated from the right side of (14), rather than the middle part. In other words, rotating the modeled magnetic field by 90° and dividing by μ_o provides the curl-free component of $\vec{J}_{\perp}$ needed to solve for the conductivity with (7) and (8).

3 Combining everything together

Figure 4 shows the results of the ionospheric conductivity calculations, along with maps of all values used to obtain these results. These additional maps provide useful and interesting information. This figure was calculated with model inputs using an IMF magnitude of 10 nT in the GSM Y-Z plane, at a clock angle orientation of 180° (entirely southward, or $B_Z = -5$), and a solar wind velocity of 450 km/s. The dipole tilt angle is 0°, and the $F_{10.7}$ index 160 sfu. Although the FAC model has the capability to use other solar indices, the ground-level magnetometer model uses only the $F_{10.7}$ index, so that is what we use.

In the top row of the figure, parts (a)-(c) shows the electric potential and the two horizontal components of the electric field. The longitudes are marked in Magnetic Local Time (MLT), in magnetic apex coordinates, with the sun at 12 noon. The gray area on the maps show the region that is outside of the cap that is used in the SCHA functions in the model. The size of this cap varies with IMF conditions. While the derivatives of the potential are calculated in northward and eastward polar coordinates, it is more useful to display the duskward and sunward components and use these in the calculations. For example, the typical electric potential pattern has a strong electric field in the duskward direction, directed from the positive peak on the dawn side toward the negative valley on the dusk side. If the northward and eastward components are shown then this pattern is not at all obvious. Minimum and maximum values of the potential and electric fields are indicated in the lower left and right corners of all contour maps, and the locations where these values are found are marked on the map with the diamond and plus symbols respectively. For clarity the levels chosen for the counter lines avoid values at exactly zero, as the contouring algorithm tends to entirely miss the zero contour around one of the two convection cells.

In the second row of Figure 4, parts (d)-(f) show the equivalent current function and the duskward and sunward components of the divergence-free currents that are calculated from the gradients of this function. Since the current flows along the direction of the contour lines, clockwise around the positive peak, the sunward component of the current flow has some resemblance to the duskward electric field. As these maps are derived from the magnetic perturbation model that covers the entire hemisphere (in magnetic apex coordinates), there is no gray boundary. The color bar scale for all horizon-

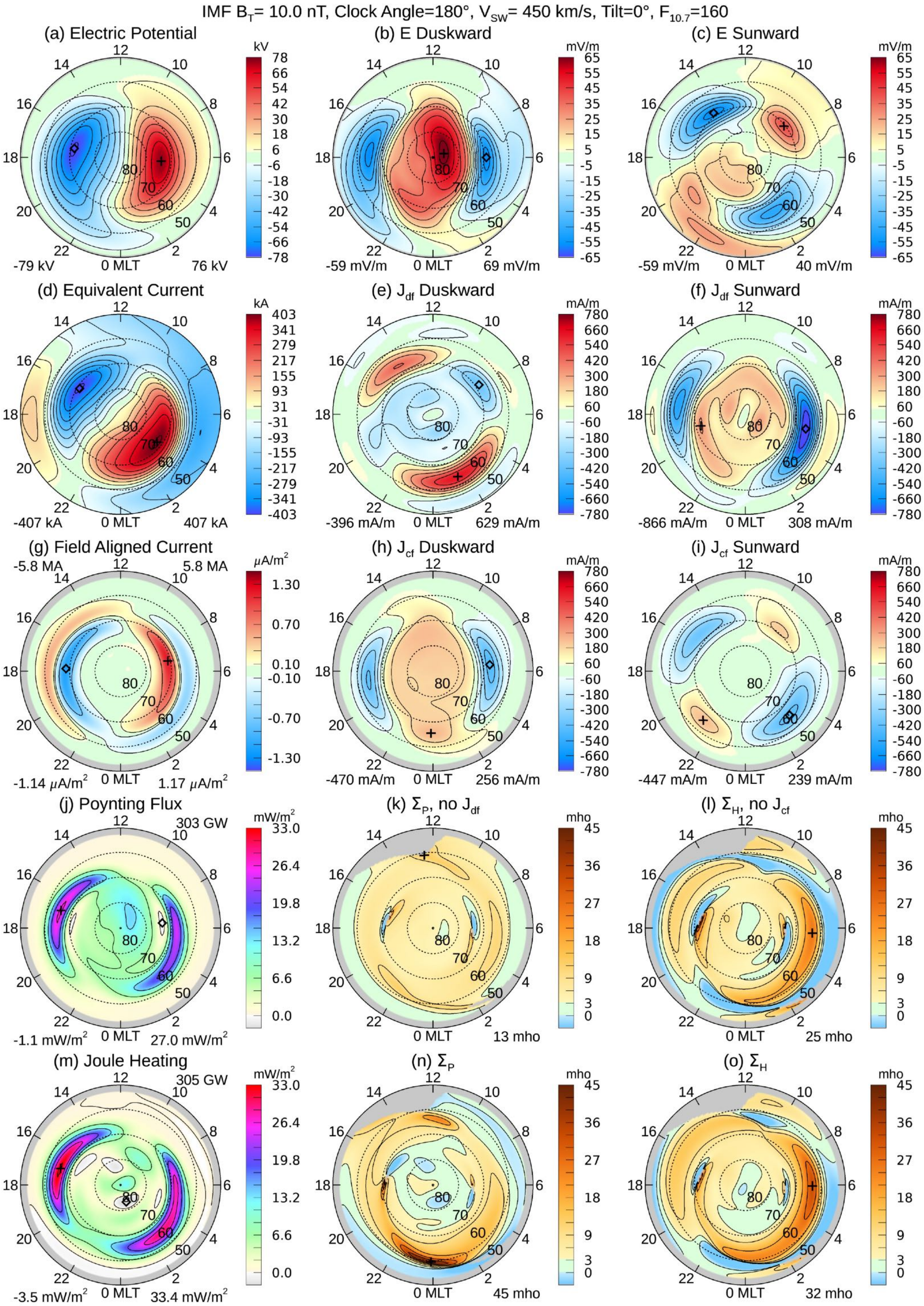

Figure 4. Conductivity input data and results, for IMF B_T magnitude 10 nT at 180° clock angle, the solar wind velocity is 450 km/s, the $F_{10.7}$ index is 160 sfu, and the dipole tilt angle is 0° corresponding to near equinox. Details are explained in the text.

tal currents is adjusted to approximately match the largest magnitude of the sunward current. Currents outside of the the electric field convection pattern appear at lower latitudes, having opposite signs. As will be seen in other examples, the patterns that are found at lower latitudes have a strong dependence on the magnitude and orientation of the IMF. This behavior leads us to assume that these reversed currents at lower latitudes are due to the magnetic effects of magnetopause and field-aligned currents, that produce a false signature of ionospheric flow in the equivalent current function.

In the third row of Figure 4, parts (g)-(i) show the field-aligned current and the duskward and sunward components of the curl-free current. Via equation (14), these currents are just the duskward and sunward magnetic fields, transposed with one sign change, and divided by μ_o. A predominately sunward magnetic field in the polar cap translates to a duskward current. These currents closely resemble the electric fields, as expected. These two components of the magnetic fields were produced directly from the SCHA functions in the FAC model, and then the FAC is calculated from their curl, equation (10). This model version (Edwards et al., 2020) had fit the spacecraft magnetic field measurements to the duskward and sunward components in order to reduce the spurious, circular harmonics in the FAC that tend to result when using polar coordinates. The total sums of the upward (negative) and downward (positive) FAC, integrated over the spherical cap, are indicated in the upper left and right corners of the contour map in units of millions of Amperes (MA). As the density of contour lines in the FAC maps tends to get too crowded around the largest values, lines are drawn only for every third interval marked on the color bar. As before, the gray area on the maps show the region outside of the SCHA cap defined by the FAC model.

The fourth row starts with the Poynting flux, 4(j), calculated from the cross product of the electric and magnetic fields. The total energy flow into the ionosphere is in the upper-right corner, in Giga-watts (GW). We note that the new electric potential and FAC models produce Poynting flux maps that we consider to be more realistic that the results from the prior models (Weimer, 2005a), with levels that are higher within the polar cap and near the cusp. Sometimes there may be a slight mismatch between the electric potential model and the FAC model (derived from independent data sets), that results in the electric and magnetic fields reversing directions at not exactly the same locations; such misalignment manifests as a negative value of the Poynting flux. These negative fluxes are simply artifacts, and colored in lighter shades of gray. In general the two models match up very well at the electric field reversals, and these areas are rather small in size and magnitude. As with the FAC map, some contour lines are omitted for clarity.

The second map in the fourth row, 4(k), shows the Pedersen conductivity that is calculated with (7), but without including the divergence-free current, from the equivalent current function. This step is included for informative, diagnostic purposes. As the calculation in (7) doesn't work where the magnitude of the electric field is very small, locations where this magnitude is small are flagged as invalid and colored in gray on the map, in addition to latitudes that are below the spherical cap of the electric field or FAC models. The limiting electric field magnitude is 3 mV/m or 7% of the peak magnitude, whichever is greater. If larger values of the limiting electric field strength are used, then the gray areas extend too much into the auroral ovals, and maybe useful conductivity values are lost.

At the electric field reversals there are small areas where conductivity may appear to be negative or have abnormally high values. Negative values are indicated with a blue coloring on the map, but these values are not considered to be realistic or meaningful. Likewise, large, positive values near the convections reversals should be ignored. In all maps of conductivity the maximum values that are indicated in the lower-right corner of the maps excluded results at latitudes greater than 68°, in order to avoid the areas around the convection reversals. The color bars on all conductivity maps have a fixed range, unlike the others that are adjusted to accommodate the largest values. A green color shows where the conductivity is greater than zero but less than 3 mho.

The next map, 4(l), shows the Hall conductivity that is calculated with (8), but without using the curl-free current from the FAC model. The format is the same as the Pedersen conductivity. In this map there are regions where the derived conductivity is negative, which is unrealistic. These areas are marked in shades of blue that darken as the value becomes more negative. While the alignment between the electric potential and equivalent current functions in 4(a) and 4(d) is generally good, on the dawn side these negative values appear where the current function reverses direction from the clockwise flow around the positive convection cell, or counter-clockwise around the negative convection cell. As we had mentioned earlier, it is thought that the reversed flows, and the unrealistic, negative conductivity values, result from interference from magnetospheric currents.

The bottom row in Figure 4 shows the results using the total currents, with the two components of the current combined together. At the left, 4(m) shows the Joule heating that is calculated with from the dot product of the electric field and this total current. The differences between the Joule heating and the Poynting flux maps will be discussed in more detail in Section 5. Finally, Figures 4(n) and 4(o) show the derived values of the Pedersen and Hall conductivities, using the total currents. The auroral oval is easily seen in these results, where the conductivity changes to values greater than 3 mho. The Hall conductivity has enhanced values near 6 MLT, that peak at 32 mho, while the largest Pedersen conductivity (45 mho) is found near midnight. The regions of higher conductivities in both maps correspond to upward field-aligned current, the blue regions in Figure 4(g), including where this FAC passes through the gap between downward current near midnight. This is a common feature in all results. On the other hand, the Pedersen conductivity that is calculated near midnight seems too large. We will return to this subject later.

4 Results from other dipole tilt and IMF clock angles

In Figures 5 and 6 are shown maps for dipole tilt angles of $-23°$ and $+23°$, corresponding to winter and summer conditions, while the zero tilt in Figure 4 corresponded to near equinox conditions. As the dipole tilt angle varies every day by about $\pm 11°$, due to the offset of the magnetic pole from the rotation axis, there is a broad range of dates when the dipole tilt angle is at the specified values; the reference to seasons does not refer to exact dates. The format of these Figures is the same as before. Both the Pedersen and Hall conductivities in 5(n) and 5(o), peak at 69 and 51 mho respectively, which are greater than for the equinox conditions. The maps for summer conditions in Figure 6 show peak Pedersen and Hall conductivities of 56 and 35 mho, that are lower than the winter values yet greater than at equinox. The positive tilt angle in the summer produces enhanced conductivities on the dayside, as expected. The enhanced Hall conductivity seen near 6 MLT in all three graphs, Figure 5(o) in particular, agrees with the results found by Green et al. (2007), in the right side of Figure 3.

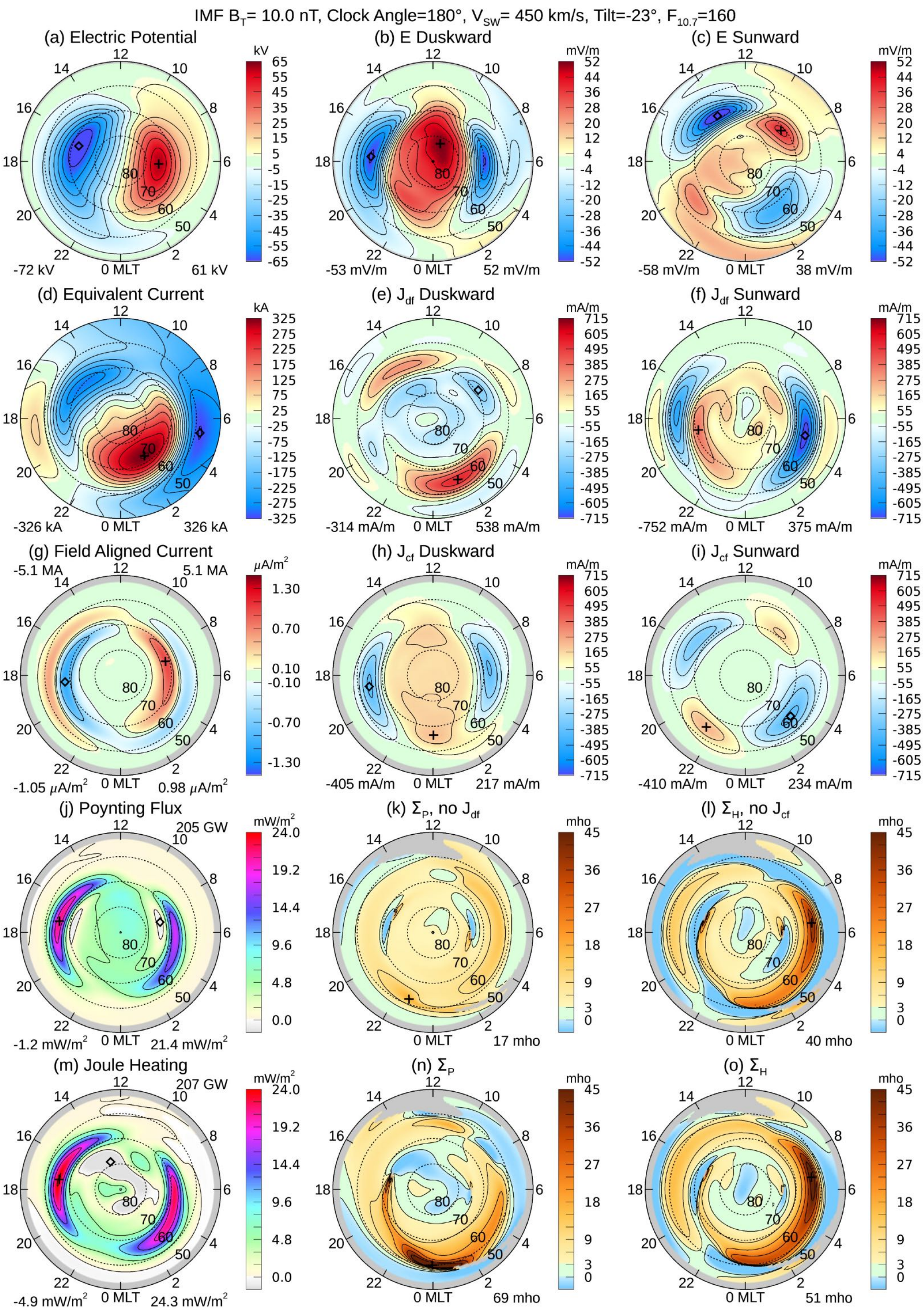

Figure 5. Conductivity input data and results for the same conditions as in Figure 4, except that the dipole tilt angle is for winter conditions. The IMF B_T magnitude is 10 nT at 180°, the solar wind velocity is 450 km/s, the $F_{10.7}$ index 160 sfu, and the dipole tilt angle is $-23°$.

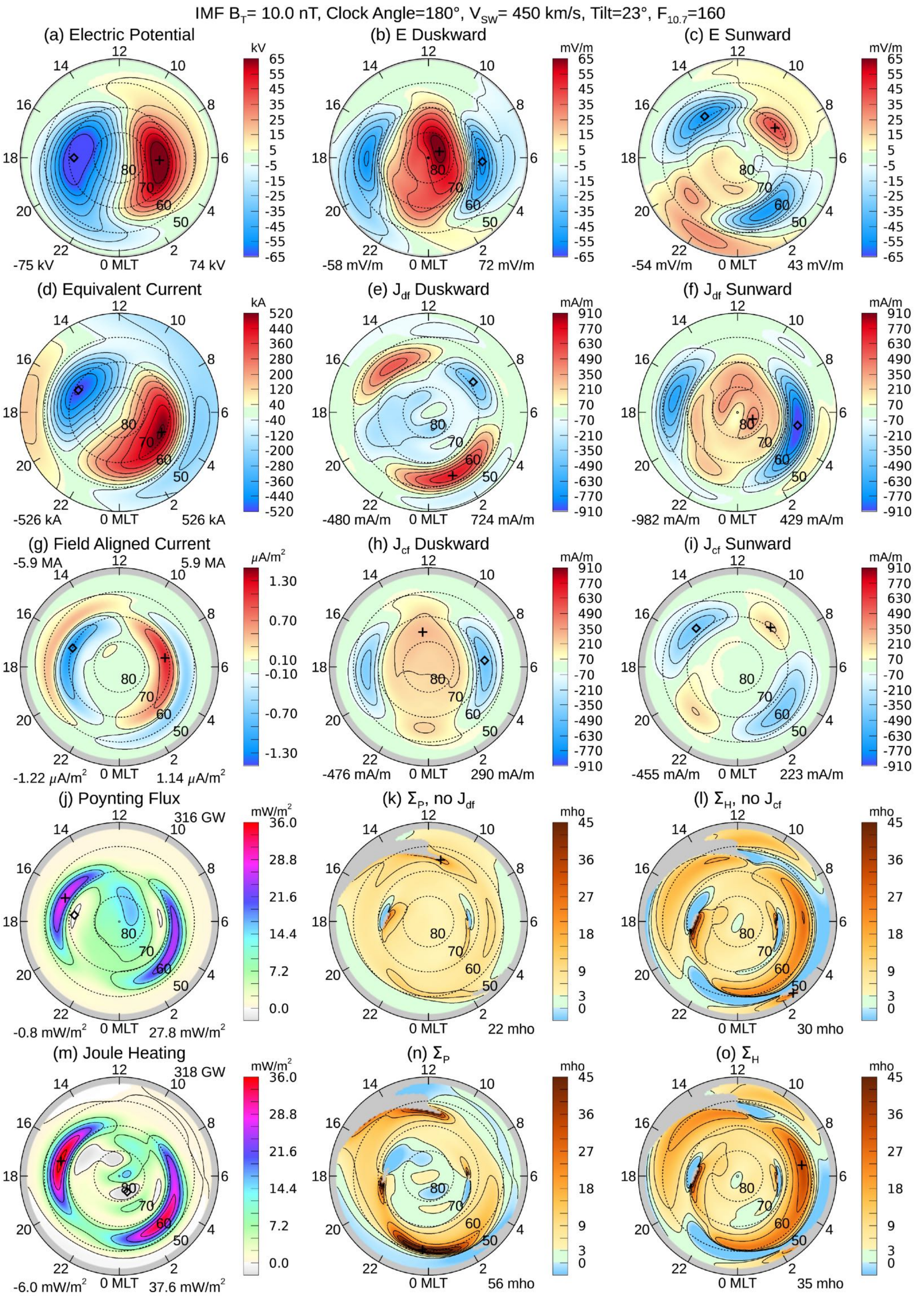

Figure 6. Conductivity input data and results for the same conditions as in Figure 4, except that the dipole tilt angle is for summer conditions. The IMF B_T magnitude is 10 nT at 180°, the solar wind velocity is 450 km/s, the $F_{10.7}$ index 160 sfu, and the dipole tilt angle is $-23°$.

One feature to note is that while the electric potentials have similar patterns in Figures 4, 5, and 6, the equivalent current function rotates as the dipole tilt angle changes, and exhibits a sharp twist near the pole under winter conditions (negative dipole tilt, Figure 5). Another noticeable feature is found near midnight, where the region of enhanced conductivities passes through the region in the electric potential patterns where the negative, dusk potential cell wraps around and under the positive cell. This warp in the electric potential patterns, known as the Harang discontinuity (Gjerloev & Hoffman, 2001; Marghitu et al., 2009), does not appear in the equivalent current functions.

Next we turn our attention to other IMF orientation angles. Figures 7 and 8 show graphs for IMF clock angles of 90° and 270°, corresponding to positive and negative values of the Y component, with $B_Z = 0$. The magnitude of the IMF is 10 nT, and the dipole tilt angle is zero, the same as in Figure 4. In both cases the conductivities are lower than when the IMF is southward (180° clock angle), with conductivity values being lowest at the 270° clock angle. In both cases the electric potentials, total FAC, and total Poynting flux are also much lower than when the clock angle is 180°. In Figure 8 the enhanced Pedersen conductivity previously seen near 0 MLT is noticeably absent. The westward electrojet is also reduced, the region of positive duskward current near 0 MLT in subplots (e) and (h) in all examples. Examples of the results for these two IMF clock angles with negative and positive tilt angles (winter and summer) are included in the Supplementary Information. The Supplement also contains a set of graphs showing the same combinations of IMF clock angle and dipole tilt angle, but with the IMF magnitude reduced from 10 to 5 nT. Similar variations in the conductivities are seen in these other examples, such as the lower values when the Y component is negative (270°).

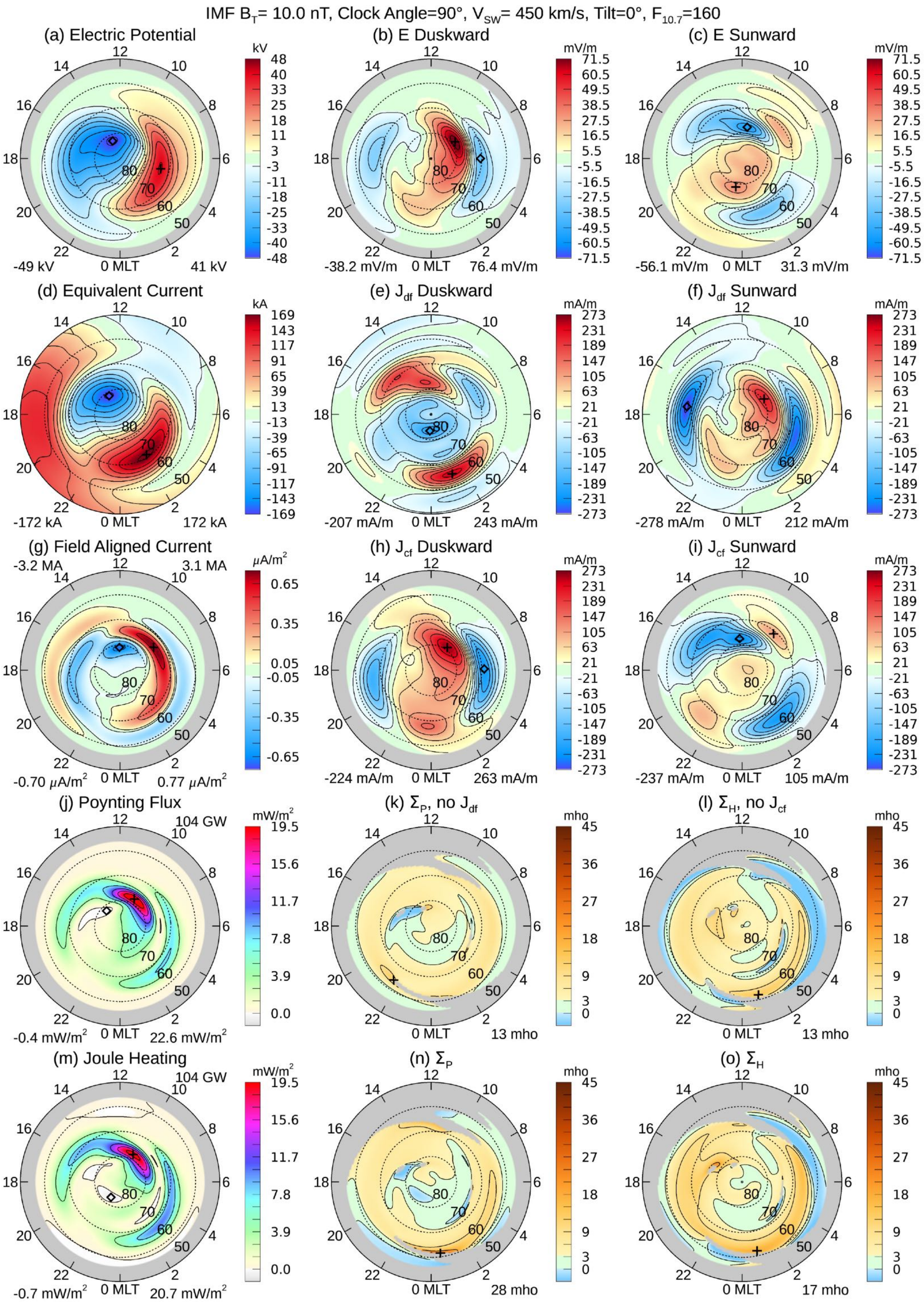

Figure 7. Conductivity input data and results for the same conditions as in Figure 4, except that IMF clock angle is changed 90°. The IMF B_T magnitude is 10 nT, the solar wind velocity 450 km/s, the $F_{10.7}$ index 160 sfu, and the dipole tilt angle is 0°.

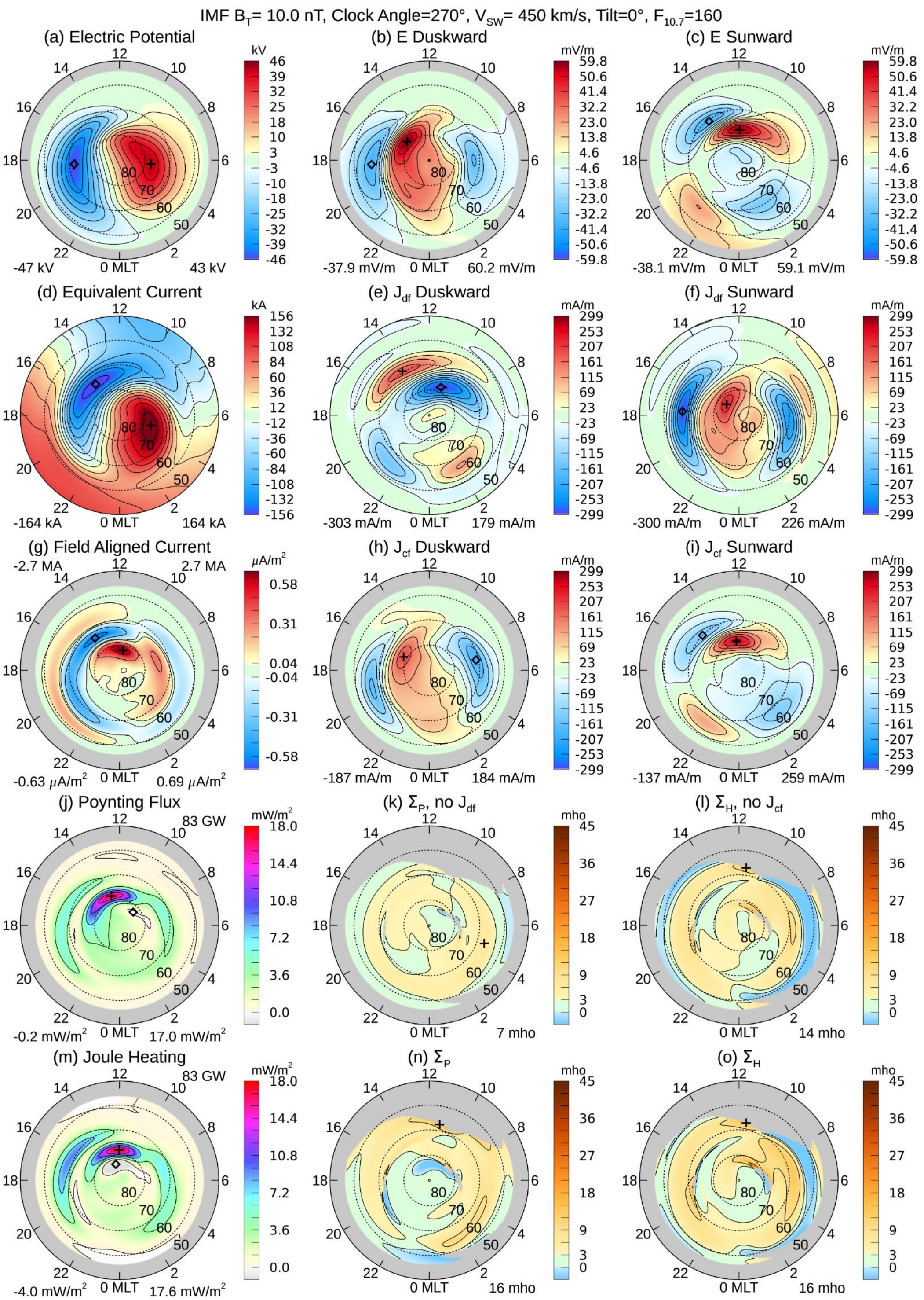

Figure 8. Conductivity input data and results for the same conditions as in Figure 4,except that IMF clock angle is changed 270°. The IMF B_T magnitude is 10 nT, the solar wind velocity 450 km/s, the $F_{10.7}$ index 160 sfu, and the dipole tilt angle is 0°.

In order to get a better comparison of how the IMF clock angle influences the conductivity values on the dawn and dusk sides, Figures 9 and 10 show the conductivity as a function of latitude at the IMF clock angles 90°, 180°, and 270°. Figure 9 shows values through a meridional slice at 4 h MLT, and Figure 10 contains results at 22 MLT. These locations avoid the artifacts at both high and low latitudes at all clock angles. The blue, green, and red lines correspond to dipole tilt angles of $-23°$, $0°$, and $+23°$, respectively. Obviously, the conductivities have an asymmetrical response to the clock angle variations. On the dawn side at 4 MLT, a 90° clock angle produces larger values than at 270°, while both are exceeded when the IMF is at 180°. The tilt angles corresponding to winter conditions (blue lines) that often have the largest values. On the dusk side (Figure 10) the southward IMF (180°) again produces the larger conductivity values, but the seasonal (tilt angle) differences are not as significant. Enhancements near 70° latitude are produced by the upward, Region 1 currents.

Figures 11 and 12 show the same type of graphs with the magnitude of the IMF reduced from 10 to 5 nT, for the purpose of demonstrating a consistent pattern. Very similar results are found, except that the conductivity values are generally lower, as expected, and there is a poleward shift to larger latitudes, due to the contraction of the auroral ovals.

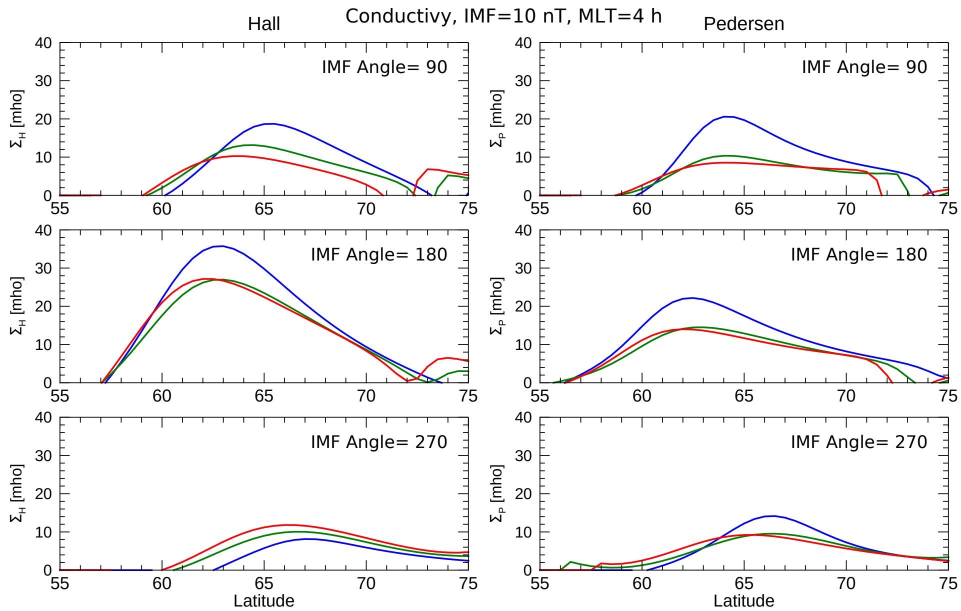

Figure 9. Conductivity as a function of latitude, at 4 hours MLT. Results are shown for an IMF magnitude of 10 nT, at IMF clock angles of 90° (top), 180° (middle), and 270° (bottom). Hall conductivity is on the left and Pedersen conductivity is on the right. The blue, green, and red lines correspond to dipole tilt angles of −23°, 0°, and +23°.

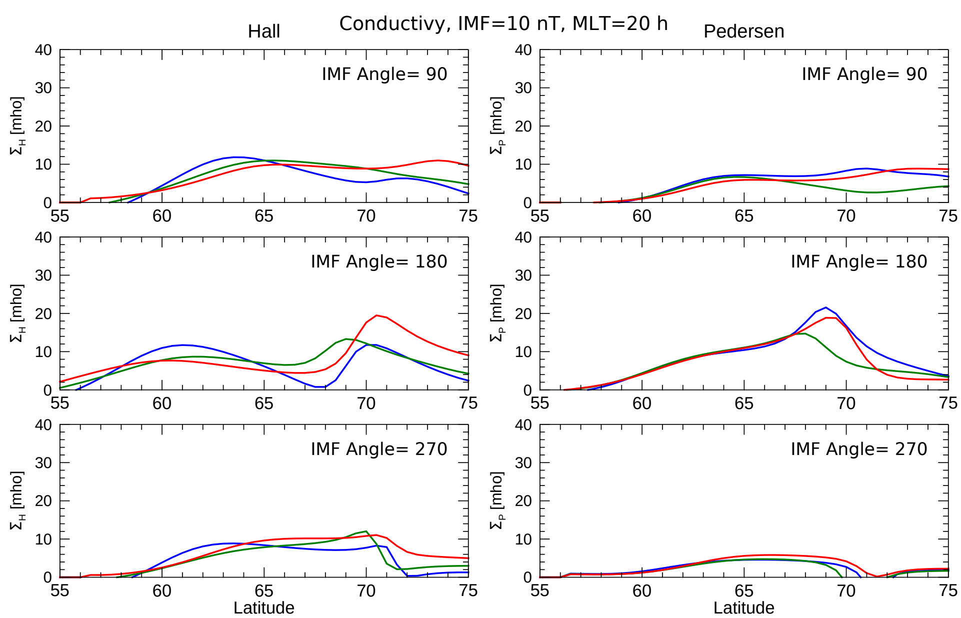

Figure 10. Conductivity as a function of latitude, at 22 hours MLT. Results are shown for an IMF magnitude of 10 nT, at IMF clock angles of 90° (top), 180° (middle), and 270° (bottom). Hall conductivity is on the left and Pedersen conductivity is on the right. The blue, green, and red lines correspond to dipole tilt angles of −23°, 0°, and +23°.

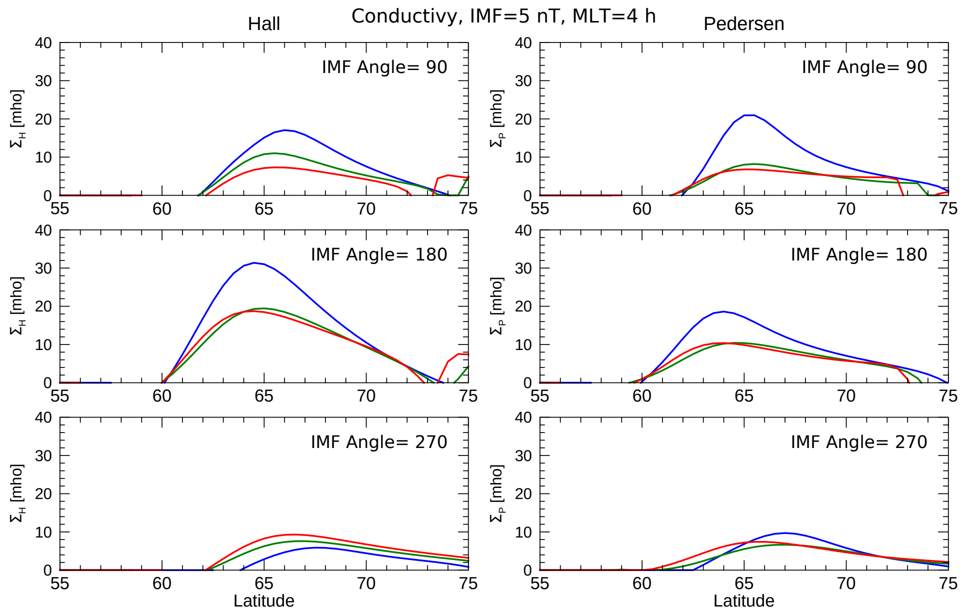

Figure 11. Conductivity as a function of latitude, at 4 hours MLT. Results are shown for an IMF magnitude of 5 nT, at IMF clock angles of 90° (top), 180° (middle), and 270° (bottom). Hall conductivity is on the left and Pedersen conductivity is on the right. The blue, green, and red lines correspond to dipole tilt angles of $-23°$, $0°$, and $+23°$.

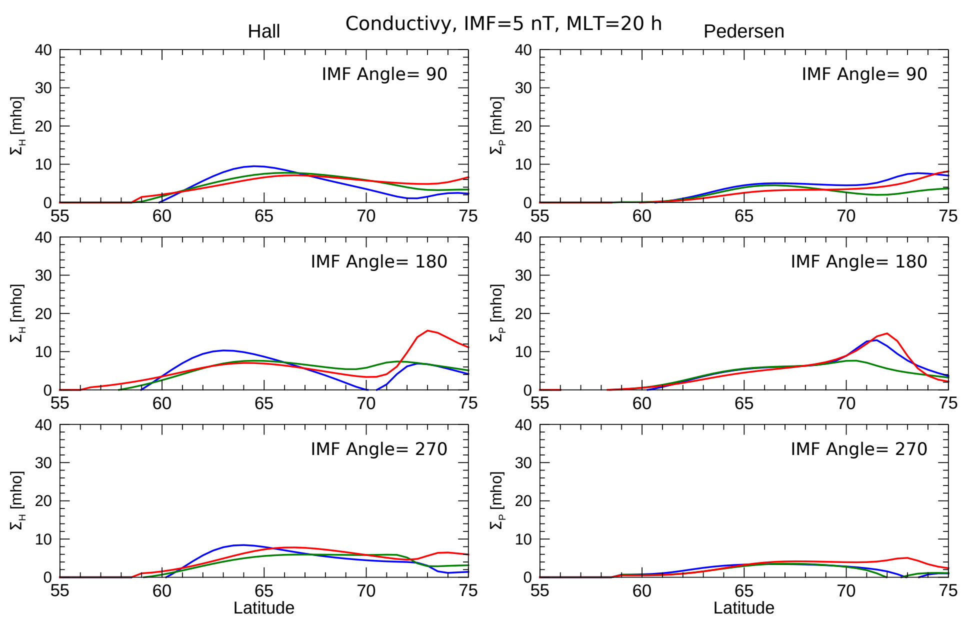

Figure 12. Conductivity as a function of latitude, at 22 hours MLT. Results are shown for an IMF magnitude of 5 nT, at IMF clock angles of 90° (top), 180° (middle), and 270° (bottom). Hall conductivity is on the left and Pedersen conductivity is on the right. The blue, green, and red lines correspond to dipole tilt angles of $-23°$, $0°$, and $+23°$.

5 Joule heating and Poynting Flux

In Figures 4 through 8 the Joule heating maps (m) are not identical to the Poynting flux distributions (j). If the dot product between the electric field and the current that is used to calculate the Joule heating uses only the curl-free components of the current, then the result is exactly identical to the Poynting flux, as shown by Weimer (2005a) and Vanhamäki et al. (2012). But if the divergence-free component is included, then the heating in some areas may not exactly match the local Poynting flux, while the integrated sum should be the same within the boundary of an electric, equipotential contour.

Such differences between the local Poynting flux and Joule heating were proposed by Richmond (2010) as the Equipotential Boundary Poynting Flux (EBPF) theorem. As explained in detail by Vanhamäki et al. (2012), when the divergence-free and curl-free parts of the ionospheric current are combined their gradients act to transport energy flux between regions, but the divergence-free component still has zero contribution to the total integrated energy flux. The energy is transferred from regions of low Pedersen conductance to regions of high conductance.

Our results show that this happening, with the Joule heating in the high-latitude polar cap tending to be lower than the Poynting flux, and greater in the auroral oval. The differences between the sums are always less than 1% of the total Poynting flux in every case, so in essence the results validate the EBPF theorem. This is the first demonstration of the theorem that uses realistic configurations of the fields and conductivities.

Some numerical error can be expected in our totals, which were derived from 19531 data points at and above 50° latitude, forming 38597 triangles on the spherical cap. Each side of the spherical triangles spans an arc length of roughly 0.5°. The values of each quantity are evaluated at the vertices, and the mean value within each triangle are multiplied with the triangle's area, and summed.

In order to more clearly demonstrate the transfer of energy flux, Figure 13 shows a map of the dot product of the electric field with the J_{df} component alone, for the same case shown in Figure 4. The energy transfer from the polar regions to auroral oval is clear. The numbers in the upper left and right corners show the totals of just the areas with negative and positive values, respectively. The dot product of the horizontal, curl-free electric field with J_{df} should integrate to zero within a boundary where the electric field

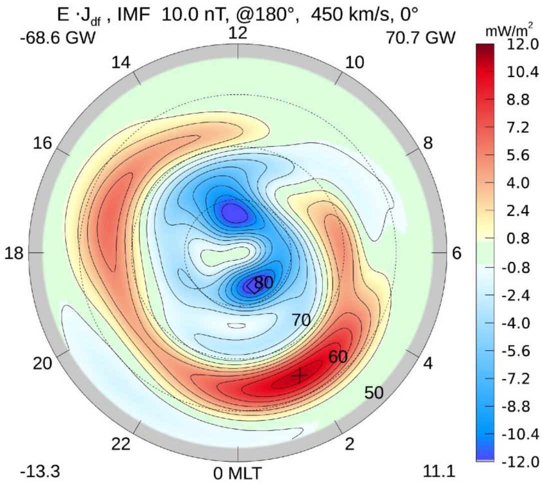

Figure 13. Dot product of electric field and divergence-free current, for the same conditions as in Figure 4. The IMF B_T magnitude is 10 nT at 180°, the solar wind velocity is 450 km/s, the $F_{10.7}$ index 160 sfu, and the dipole tilt angle is 0°. The integrated sum of all negative values is indicated in the upper left corner, and this total for all positive values in indicated in the upper right corner, in units of GigaWatts.

and J_{df} both go to zero. A non-zero sum could result if the divergence-free current does not exactly go to zero at the electric potential boundary, which is true in our case, or indicate that J_{df} is not perfectly divergence-free. As the 2 GW difference is only 0.7% of the 303 GW total Poynting flux, such errors are small.

Another possibility for the difference is that due to the effect of the neutral winds, the effective electric field in the ionosphere is lower than predicted with the electric field model alone. The actual Joule heating would then be lower than what is calculated. The Poynting flux that is obtained from electric and magnetic field measurements far above the ionosphere has no such interference from neutral winds, although the winds can influence the total amount of energy that the ionosphere draws from the magnetosphere.

6 Discussion

The application of the formulas by Amm (2001) to calculate the ionospheric Pedersen and Hall conductivities, using our three, separate empirical models as the input, has produced new maps of these conductivities for various conditions. The electric potential, equivalent current, and field-aligned current maps in every case provide useful and interesting results.

For the most part, the values of the conductivities that are produced seem reasonable. Enhanced conductivities in the auroral ovals are seen, as expected, with values in the range of 3 to 9 mhos under moderate conditions, with some regions having substantial enhancements on top of that. At positive and negative values of the Y component of the IMF the conductivity results are very different. This is significant, since the existing statistical models of conductivity do not account for the orientation of the IMF. Some of the conductivity values that we found seem to be greater than what are produced with existing models. Both the Hall and Pedersen conductivities are higher for winter, or negative dipole tilt, conditions, particularly on the dawn side and toward midnight. There are some gaps and artifacts produced where the various models don't exactly line up. Various forces produce equivalent current signatures at lower latitudes that cause the conductivity to seem negative, values that are not realistic. Magnetospheric currents are one possible source of uncertainty here. The correction that was employed to compensate for the ring current actually had little effect on these results, with differences in the maximum values on the order of 2 mho if the correction was either removed or doubled, so that adjustment doesn't seem to be an issue.

The accuracy of the results is difficult to ascertain with reasonable certainty. All three statistical models provide a large-scale representation of the electric and magnetic field variations. As they are global models there is considerable smoothing of the small-scale fluctuations contained in the measurements. These variations are a mixture of fields and currents that may persist only for a brief period of time, or move from one location to another. Such fluctuations produce standard deviations that seem large. For example, the publication by Weimer (2013) contains illustrations of model predictions compared with measured magnetic fields as a function of time at various locations. The predictions reproduce very well the low frequency variations, but not the high-frequency fluctuations that are superimposed. Another figure shows the mean absolute model errors when the IMF magnitude is in the range of 12 to 20 nT. At auroral latitudes in the 3 to 6 MLT sector the mean error of the northward component is about 140 nT, or 56% of the mean magnitude. For another example, the development of the FAC model (Edwards et al., 2020) involved grouping together all of the measurements taken under similar conditions and using SCHA to fit the sunward and duskward components of the magnetic field. For conditions most similar to our Figure 4 the standard deviations of the fits were 123 and 111 nT for the sunward and duskward components, about 20% of the peak magnitudes in the model's final output. Of course, our smoothed calculations of the conductivities do not include the small-scale enhancements that occur within the auroral arcs that are non-stationary in time and space.

One persistent feature in the results is the presence of the extraordinarily large Pedersen conductivities in a narrow band near midnight. A close examination of the map data shows that the peak value occurs in a region of low electric field strength, exactly where the sunward electric field at midnight passes through zero while changing sign from negative to positive, as latitude decreases. The curl-free, sunward current changes sign also, about one-half of a degree to the north. The duskward electric field is weak, around 5 mV/m. There is a rather strong (> 200 mA/m) divergence-free (equivalent) current here in the duskward direction, part of the westward, electrojet. This Hall current does not change sign with the electric field, which results in the derived Hall conductivity changing signs from positive to negative. This same pattern is found often, and in association with the Harang region where the negative, dusk electric potential cell wraps around the positive cell near midnight, on the lower-latitude side (Gjerloev & Hoffman, 2001; Marghitu et al., 2009). When the IMF is in the -Y direction (Figure 8, 270° orientation) the extra large Pedersen conductivity is not present, the signature of the Harang discontinuity is weak, and the westward (duskward) currents at midnight are substantially lower.

Shue and Weimer (1994) had proposed that polarization electric fields around areas of enhanced conductivity are responsible for forming the Harang discontinuity; the effect is to block the divergence of Hall currents where there are gradients in the Hall conductivity. Further evidence of this concept has been provided by Nakamizo and Yoshikawa (2019), and our results are consistent with this hypothesis. It seems that equations (7) and (8) are not accurate where there are conductivity gradients. The derived conductivity values near midnight, from 22 to 2 MLT, should not be trusted.

A significant result is the demonstration of the predictions of the EBPF theorem by Richmond (2010). In the past only idealized examples have been shown, including the results by Vanhamäki et al. (2012). This is the first verification with realistic configurations of Poynting flux and conductivity. According to this theorem, the distribution of the Poynting flux may not match the Joule heating that occurs below, with a horizontal redistribution of energy taking place, perhaps to locations some distance from the Poynting flux; within the boundary of an enclosing equipotential contour the totals are the same. Evidence for this redistribution taking place is seen in the differences between our Poynting flux and Joule heating maps, in which Poynting flux at high latitudes goes to slightly elevated levels of Joule heating in the auroral ovals where the conductivity is greater. Our results do have some differences in the total, integrated energy, but the fractional amount of the differences are relatively minor.

The effects of the neutral winds, which are difficult to measure, are not included in these results. We note that Vasyliūnas and Song (2005) report that the Joule heating "as conventionally defined is not primarily Ohmic or Joule heating in the physical sense but is for the most part simply frictional heating from the relative motion of plasma and neutrals." Thayer (1998) indicates that a neutral wind in the direction of the $\mathbf{E}\times\mathbf{B}$ vector will decrease the Joule heating rate, while a component of the neutral wind in the opposite direction will act to increase it. His observations in one particular time period indicated that the neutral winds could reduce the local Joule heating rate by over 75% in the upper E region while enhancing the local heating rate by nearly 50% in the lower E region, with an overall decrease of 40% in the height-integrated values. If the electric field is in a steady direction then the neutral winds act to reduce the Joule heating rate, but if the electric fields change directions suddenly then the effect is reversed (Thayer, 1998).

Billett et al. (2018) report that the reduction in the Joule heating due to the neutral winds primarily happens at high magnetic latitudes and in the dusk sector. They report on observations showing a persistent absence of a neutral winds in the dawn circulation cell, and hence a lower reduction. They report that "the percentage contribution of the wind correction to the area-integrated Joule heating rate can vary by ±14% depending on season and geomagnetic activity level," with a greater influence occurring in the hemispheric winter months.

While our results do not include the effects of the neutral winds, they do show how the currents and electric fields are related to each other under typical conditions, which implicitly includes whatever influence the neutral winds may have. The conductivity values obtained with the electrodynamic models could be what numerical modelers actually need in order to compute currents from the electric potentials, or vice versa, if the neutral winds are not available.

7 Summary

We have used a combination of empirical models for the electric potentials, field-aligned current, and ground-level magnetic perturbations to obtain estimates of the height-integrated Pedersen and Hall conductivities, using the formulas presented by Amm (2001) and demonstrated by Green et al. (2007). Maps of the high-latitude, ionospheric conductivities were derived for varying combinations of the dipole tilt angle, IMF magnitude, and IMF orientation angle in the GSM Y-Z plane. Two components of the total ionospheric current were combined, a "curl-free" component that is generally associated with Pedersen currents, and a "divergence-free" component that is usually associated with Hall currents. While some of the results should be very useful, there are places where the technique fails. The findings are summarized as follows:

1. The auroral ovals are recognizable in the maps, as an increase in the conductivity to values greater than three mhos.

2. Inclusion of the divergence-free component from the equivalent current function in the calculation leads to significantly greater conductivity values.

3. Reversing the sign of the Y component of the IMF results in substantially different conductivity patterns, with values that are lower when B_Y is negative. Changes in the dipole tilt angle also have a significant influence. These factors need to be considered in all future conductivity models that may be derived from particle precipitation measurements.

4. The Pedersen conductivities have unusually large values near midnight, especially with negative dipole tilt angles, that are colocated with the Harang discontinuity in the electric potential patterns. The electric field strength is very low here, and the equivalent currents typically do not have features that match the curves in the electric potential patterns. We conclude that the results that are obtained at MLT values within 2 hours of midnight should not be trusted at face value. This region requires further investigation, at resolutions greater than presently available. One outstanding question is why the electric potential and equivalent current patterns behave as they do in the Harang region.

5. At positive dipole tilt angles, larger Pedersen and Hall conductivities are produced by the calculations on the day side around noon. However, the results in this area are also suspect, for the same reasons given for midnight.

6. The Hall conductivities are largest on the dawn side in the upward, Region 2 field-aligned currents near 6 MLT, and enhanced Hall conductivities are also found where this upward current wraps around at midnight through the Harang discontinuity, especially with negative dipole tilt.

7. On the dusk side the Hall conductivity is also elevated within the Region 2 current, but not as much as on the dawn side.

8. The dipole tilt angle has a strong influence on the equivalent current functions. Going from positive to negative tilt, the equivalent current pattern rotate clockwise, and kinks or twists within the polar cap at negative tilt, assumed to be a terminator effect.

9. There are features in the equivalent currents, that are derived from ground-level magnetic field values, that interfere with conductivity derivation. Equivalent currents are present at on the dawn and dusk sides at low latitudes, outside of the the electric field convection pattern, but with reversed signs. These patterns have a strong dependence on the magnitude and orientation of the IMF. Their presence in steady-state conditions and at low levels of IMF magnitude preclude penetration electric fields. This behavior leads us to assume that these reversed currents at lower latitudes are due to the magnetic effects of magnetopause and field-aligned currents, that produce a false signature of ionospheric flow in the equivalent current function. This topic is another that requires further investigation.

10. Using both components of the ionospheric currents to calculate the Joule heating produces mappings that are not identical to the Poynting flux. The Poynting flux often has energy flow at high latitudes and near noon that are reduced in the Joule heating maps, reappearing as slightly enhanced levels of Joule heating within the auroral ovals where the conductivity is greater. The differences between the Poynting flux and Joule heat distribution are not great. The integrated sums within the zero equipotential boundary are nearly the same, to within 1% of the total. These results confirm the predictions of the Equipotential Boundary Poynting Flux theorem by Richmond (2010), for the first time with realistic conductivity distributions.

Acknowledgments

Daniel Weimer and Thom Edwards were supported by NSF grants AGS-1638270 and PLR-1543364 to Virginia Tech, with additional support from a subcontract to Hampton University, on NASA grant NNX15AE05G. The authors thank Art Richmond for helpful comments on an earlier version of the manuscript.

An archive of graphs and data can be found at `https://bit.ly//36fbff0`. (Later on, this archive will be moved from Google to an immutable archive at Zenodo.org) This archive includes reproductions of Figures 4 to 8 all figures in the Supplement, but arranged in a horizontal, landscape format for easier viewing on a computer screen. Maps of the dot product of the electric field and divergence-free current in each case are also included as well as the equivalent current functions down to a latitude of 35°. The archive contains the ground-level magnetic field values that are used to calculate the equivalent currents, and the resulting spherical harmonic coefficients. The SCHA coefficients from the electric potential and FAC models are included for every case, as well as digital files containing the conductivity results. Data used in the development of the magnetic perturbation model are available through Weimer et al. (2010) and Weimer (2013). Data used in the development of the field-aligned current model are available through Edwards et al. (2020). The electric potential model (Edwards, 2019) was developed with the Swarm crosstrack ion drift data available at `http://earth.esa.int/swarm/` and Dynamics Explorer-2 Vector Electric Field measurements at `https://cdaweb.gsfc.nasa.gov/`. All models used solar wind and IMF measurements from the ACE satellite, at `https://cdaweb.gsfc.nasa.gov/`.

References

Ahn, B.-H., Richmond, A. D., Kamide, Y., Kroehl, H. W., Emery, B. A., de la Beaujardiere, O., & Akasofu, S.-I. (1998). An ionospheric conductance model based on ground magnetic disturbance data. *J. Geophys. Res.*, *103*(A7), 14769-14780. doi: 10.1029/97JA03088

Amm, O. (1995). Direct determination of the local ionospheric Hall conductance distribution from two-dimensionalelectric and magnetic field data: Application of the method using models of typical ionospheric electrodynamic situations. *J. Geophys. Res.*, *100*(A11), 21473–21488. doi: 10.1029/95JA02213

Amm, O. (1997). Ionospheric elementary current systems in spherical coordinates and their application. *J. Geomag. Geoelectr.*, *49*(7), 947–955. doi: 10.5636/jgg.49.947

Amm, O. (1998). Method of characteristics in spherical geometry applied to a Harang-discontinuity situation. *Annales Geophysicae*, *16*(4), 413–424. doi: 10.1007/s00585-998-0413-2

Amm, O. (2001). The elementary current method for calculating ionospheric current systems from multisatellite and ground magnetometer data. *J. Geophys. Res.*, *106*(A11), 24843–24856. doi: 10.1029/2001JA900021

Amm, O., Aruliah, A., Buchert, S. C., Fujii, R., Gjerloev, J. W., Ieda, A., ... Yoshikawa, A. (2008). Towards understanding the electrodynamics of the 3-dimensional high-latitude ionosphere: present and future. *Ann. Geophys.*, *26*, 3913–3932. doi: 10.5194/angeo-26-3913-2008

Amm, O., Vanhamäki, H., Kauristie, K., Stolle, C., Christiansen, F., Haagmans, R., ... Escoubet, C. P. (2015). A method to derive maps of ionospheric conductances, currents, and convection from the Swarm multisatellite mission. *Journal of Geophysical Research: Space Physics*, *120*(4), 3263–3282. doi: 10.1002/2014JA020154

Amm, O., & Viljanen, A. (1999). Ionospheric disturbance magnetic field continuation from the ground to the ionosphere using spherical elementary currents systems. *Earth Planets Space*, *51*, 431–440. doi: 10.1186/BF03352247

Backus, G. (1986). Poloidal and toroidal fields in geomagnetic field modeling. *Rev. Geophys.*, *24*, 75.

Bilitza, D. (2001). International reference ionosphere 2000. *Radio Science*, *36*(2), 261–275.

Billett, D. D., Grocott, A., Wild, J. A., Walach, M.-T., & Kosch, M. J. (2018). Diurnal variations in global joule heating morphology and magnitude due to neutral winds. *Journal of Geophysical Research: Space Physics*, *123*(3), 2398–2411. doi: 10.1002/2017JA025141

Brekke, A. (2013). *Physics of the upper polar atmosphere* (Second ed.). Berlin, Heidelberg: Springer Berlin Heidelberg. doi: 10.1007/978-3-642-27401-5

Brekke, A., & Moen, J. (1993). Observations of high latitude ionospheric conductances. *J. Atmos. Sol. Terr. Phys.*, *55*(11), 1493-1512.

Chapman, S., & Bartels, J. (1940). *Geomagnetism* (Vols. Vol. II, Analysis of the data, and physical theories). London: Oxford University Press.

Edwards, T. R. (2019). *A new suite of ionospheric electrodynamics models* (PhD thesis). Virginia Polytechnic Institute and State University.

Edwards, T. R., Weimer, D. R., Olsen, N., Lühr, H., Tobiska, W. K., & Anderson, B. J. (2020). A third generation field-aligned current model. *J. Geophys. Res. Space Physics*, *125*(2019JA027249). doi: 10.1029/2019JA027249

Fuller-Rowell, T. J., & Evans, D. S. (1987). Height-integrated Pedersen and Hall conductivity patterns inferred from the TIROS-NOAA satellite data. *J. Geophys. Res.*, *92*(A7), 7606-7618.

Galand, M., & Richmond, A. (2001). Ionospheric electrical conductances produced by auroral proton precipitation. *J. Geophys. Res.*, *106*(A1), 117-125.

Gjerloev, J. W., & Hoffman, R. A. (2001). The convection electric field in auroral substorms. *Journal of Geophysical Research: Space Physics*, *106*(A7), 12919-12931. doi: 10.1029/1999JA000240

Green, D. L., Waters, C. L., Korth, H., Anderson, B. J., Ridley, A. J., & Barnes, R. J. (2007). Technique: Large-scale ionospheric conductance estimated from combined satellite and ground-based electromagnetic data. *J. Geophys. Res.*, *112*(A05303). doi: 10.1029/2006JA012069

Haines, G. (1988). Computer programs for spherical cap harmonic analysis of potential and general fields. *Computers and Geosciences*, *14*(4), 413–447. doi: 10.1016/0098-3004(88)90027-1

Haines, G. V. (1985). Spherical cap harmonic analysis. *J. Geophys. Res.*, *90*(B3), 2583. doi: 10.1029/JB090iB03p02583

Haines, G. V., & Torta, J. M. (1994). Determination of equivalent current sources from spherical cap harmonic models of geomagnetic field variations. *Geophys. Res. Int.*, *118*(3), 499-514. doi: 10.1111/j.1365-246X.1994.tb03981.x

Hardy, D. A., Gussenhoven, M. S., Raistrick, R., & McNeil, W. J. (1987). Statistical and functional representations of the patterns of auroral energy flux, number flux, and conductivity. *J. Geophys. Res.*, *92*, 12275.

Hedin, A. E. (1991). Extension of the MSIS thermosphere model into the middle and lower atmosphere. *J. Geophys. Res.*, *96*, 1159.

Kamide, Y., Richmond, A. D., & Matsushita, S. (1981). Estimation of ionospheric electric fields, ionospheric currents, and field-aligned currents from ground magnetic records. *Journal of Geophysical Research*, *86*(A2), 801–813. doi: 10.1029/JA086iA02p00801

Lomidze, L., Burchill, J. K., Knudsen, D. J., Kouznetsov, A., & Weimer, D. R. (2019). Validity study of the swarm horizontal cross-track ion drift velocities in the high-latitude ionosphere. *Earth and Space Science*, *6*(3), 411-432. doi: 10.1029/2018EA000546

Lummerzheim, D., Rees, M. H., Craven, J. D., & Frank, L. A. (1991). Ionospheric condactances derived from de-1 aurora1 images. *J. Atmos. Terr. Phys.*, *53*(3–4), 281–292.

Mallinckrodt, A. J. (1985). A numerical simulation of auroral ionospheric electrodynamics. *J. Geophys. Res.*, *90*(A1), 409–417. doi: 10.1029/JA090iA01p00409

Marghitu, O., Karlsson, T., Klecker, B., Haerendel, G., & McFadden, J. (2009). Auroral arc and oval electrodynamics in the harang region. *Journal of Geophysical Research: Space Physics*, *114*(A3). doi: 10.1029/2008JA013630

Matsushita, S. (1975). Morphology of slowly-varying geomagnetic external fields – a review. *Physics of the Earth and Planetary Interiors*, *10*, 299–312. doi: 10.1016/0031-9201(75)90056-4

Nakamizo, A., & Yoshikawa, A. (2019). Deformation of ionospheric potential pattern by ionospheric hall polarization. *Journal of Geophysical Research: Space Physics*, *124*(9), 7553–7580. doi: 10.1029/2018JA026013

Picone, J., Hedin, A., Drob, D., & Aikin, A. (2002). NRLMSISE-00 empirical model of the atmosphere: Statistical comparisons and scientific issues. *J. Geophys. Res.*, *107*(A12). doi: 10.1029/2002JA009430

Prölss, G. W., & Bird, M. K. (2004). *Physics of the earth's space environment: an introduction*. Springer-Verlag Berlin Heidelberg. (ISBN 3-540-21426-7)

Rasmussen, C. E., Schunk, R. W., & Wickwar, V. B. (1988). A photochemical equilibrium model for ionospheric conductivity. *jgr*, *93*(A9), 9831–9840.

Rees, M. H. (1989). *Physics and chemistry of the upper atmosphere.* New York: Cambridge Univ. Press.

Richmond, A. D. (1995a). Ionospheric electrodynamics. In H. Volland (Ed.), *Handbook of atmospheric electrodynamics, vol. 2* (pp. 249–290). CRC Press, Boca Raton, Fla.

Richmond, A. D. (1995b). Ionospheric electrodynamics using magnetic apex coordinates. *J. Geomag. Geoelectr.*, *47*, 191. doi: 10.5636/jgg.47.191

Richmond, A. D. (2010). On the ionospheric application of poynting's theorem. *Journal of Geophysical Research: Space Physics*, *115*(A10). doi: 10.1029/2010JA015768

Richmond, A. D., & Kamide, Y. (1988). Mapping electrodynamic features of the high-latitude ionosphere from localized observations: technique. *J. Geophys. Res.*, *93*(A6), 5741–5759. doi: 10.1029/JA093iA06p05741

Ridley, A. J., Gombosi, T. I., & DeZeeuw, D. L. (2004). Ionospheric control of the magnetosphere: Conductance. *Annales Geophysicae*, *22*(2), 567–584.

Robinson, R. M., Vondrak, R. R., Miller, K., Babbs, T., & Hardy, D. (1987). On calculating ionospheric conductances from the flux and energy of precipitating electrons. *J. Geophys. Res.*, *92*, 2565.

Ruohoniemi, J. M., & Greenwald, R. A. (1996). Statistical patterns of high-latitude convection obtained from Goose Bay HF radar observations. *J. Geophys. Res.*, *101*, 21743–21763. doi: 10.1029/96JA01584

Ruohoniemi, J. M., & Greenwald, R. A. (2005). Depenencies of highlatitude plasma convection: Consideration of interplanetary magnetic field, seasonal, and universal time factors in statistical patterns. *J. Geophys. Res.*, *110*(A09204). doi: 10.1029/2004JA010815

Shue, J.-H., & Weimer, D. R. (1994). The relationship between ionospheric convection and magnetic activity. *J. Geophys. Res. Space Physics*, *99*(A1), 401–415. doi: 10.1029/93JA01946

Thayer, J. P. (1998). Height-resolved Joule heating rates in the high-latitude E region and the influence of neutral winds. *Journal of Geophysical Research: Space Physics*, *103*(A1), 471–487. doi: 10.1029/97JA02536

Vanhamäki, H., Yoshikawa, A., Amm, O., & Fujii, R. (2012). Ionospheric joule heating and poynting flux in quasi-static approximation. *Journal of Geophysical Research: Space Physics*, *117*(A8). doi: 10.1029/2012JA017841

VanZandt, T. E., Clark, W. L., & Warnock, J. M. (1972). Magnetic apex coordinates: A magnetic coordinate system for the ionospheric f_2 layer. *J. Geophys. Res.*, *77*, 2406. doi: 10.1029/JA077i013p02406

Vasyliūnas, V. M., & Song, P. (2005). Meaning of ionospheric Joule heating. *J. Geophys. Res.*, *110*. doi: 10.1029/2004JA010615

Weimer, D. R. (2005a). Improved ionospheric electrodynamic models and application to calculating Joule heating rates. *J. Geophys. Res.*, *110*. doi: 10.1029/2004JA010884

Weimer, D. R. (2005b). Predicting surface geomagnetic variations using ionospheric electrodynamic models. *J. Geophys. Res.*, *110*. doi: 10.1029/2005JA011270

Weimer, D. R. (2013). An empirical model of ground-level geomagnetic perturbations. *Space Weather*, *11*, 107–120. doi: 10.1002/swe.20030

Weimer, D. R. (2019). Derivation of hemispheric ionospheric current functions from ground-level magnetic fields. *J. Geophys. Res. Space Physics*, *124*(2018JA026191). doi: 10.1029/2018JA026191

Weimer, D. R., Clauer, C. R., Engebretson, M. J., Hansen, T. L., Gleisner, H., Mann, I., & Yumoto, K. (2010). Statistical maps of geomagnetic perturbations as a function of the interplanetary magnetic field. *J. Geophys. Res.*, *115*. doi: 10.1029/2010JA015540

Wiltberger, M., Wang, W., Burns, A. G., Solomon, S. C., Lyon, J. G., & Goodrich, C. C. (2004). Initial results from the coupled magnetosphere ionosphere thermosphere model: Magnetospheric and ionospheric responses. *J. Atmos. Sol. Terr. Phys.*, *66*, 1411.

Yamazaki, Y., & Maute, A. (2017). Sq and EEJ–A review on the daily variation of the geomagnetic field caused by ionospheric dynamo currents. *Space Science Reviews*, *206*(1). doi: 10.1007/s11214-016-0282-z

Supporting Information for "Ionospheric Conductances Derived From Electrodynamic Models"

D. R. Weimer[1,2] and Thom R. Edwards[3]

[1]Center for Space Science and Engineering Research, Virginia Tech, Blacksburg, Virginia, USA

[2]National Institute of Aerospace, Hampton, Virginia, USA

[3]Danish Technical University, Copenhagen, Denmark

Contents of this file

Introduction

This Supporting Information contains 13 additional figures that supplement the figures included in the main body of the paper. Figures S1–S4 show input values and conductivity results for dipole tilt angles of −23° and +23° for the Interplanetary Magnetic Field (IMF) clock angles of 90° and 270°, with an IMF magnitude of 10 nT. Figures S5–S13 show the same maps but for an IMF magnitude of 5 nT, for three dipole tilt angles (−23°, 0° , +23°) at three IMF clock angles 90°, 180° , 270°). In all figures the solar wind velocity is 450 km/s and the $F_{10.7}$ index is 160 sfu. The format is the same as Figures 4–8 in the paper:

In the top row of each figure, maps (a)-(c) shows the electric potential and the two horizontal components of the electric field. The longitudes are marked in Magnetic Local Time (MLT), in magnetic apex coordinates, with the sun at 12 noon. The gray area on the maps show the region that is outside of the cap that is used in the SCHA functions in the model. Minimum and maximum values of the potential and electric fields are indicated in the lower left and right corners of all contour maps, and the locations where these values are found are marked on the map with the diamond and plus symbols respectively.

In the second row of these figures, maps (d)-(f) show the equivalent current function and the duskward and sunward components of the divergence-free currents that are calculated from the gradients of this function. The color bar scale for all horizontal currents is adjusted to approximately match the largest magnitude of the sunward current.

In the third row, map (g) shows the field-aligned current (FAC) and (h)-(i) show the duskward and sunward components of the curl-free current. Lines are drawn only for every third interval marked on the color bar to reduce crowding around the peaks. The gray area on the maps show the region outside of the boundaries of the FAC model. The total sums of the upward (negative) and downward (positive) FAC, integrated over the spherical cap, are indicated in the upper left and right corners of the contour map in units of millions of Amperes (MA).

The fourth row starts with the Poynting flux, (j), calculated from the cross product of the electric and magnetic fields. The total energy flow into the ionosphere is in the upper-right corner, in Giga-watts (GW). The second map in the fourth row, (k), shows the Pedersen conductivity that is calculated without use of the divergence-free component of the horizontal current. Map (l) shows the Hall conductivity that is calculated without use of the curl-free current.

The map at the left in the bottom row, (m) shows the Joule heating that is calculated with from the dot product of the electric field and the total current. Maps (n) and (o) in the bottom row show the final values of the Pedersen conductivity and Hall conductivities, derived using the total currents.

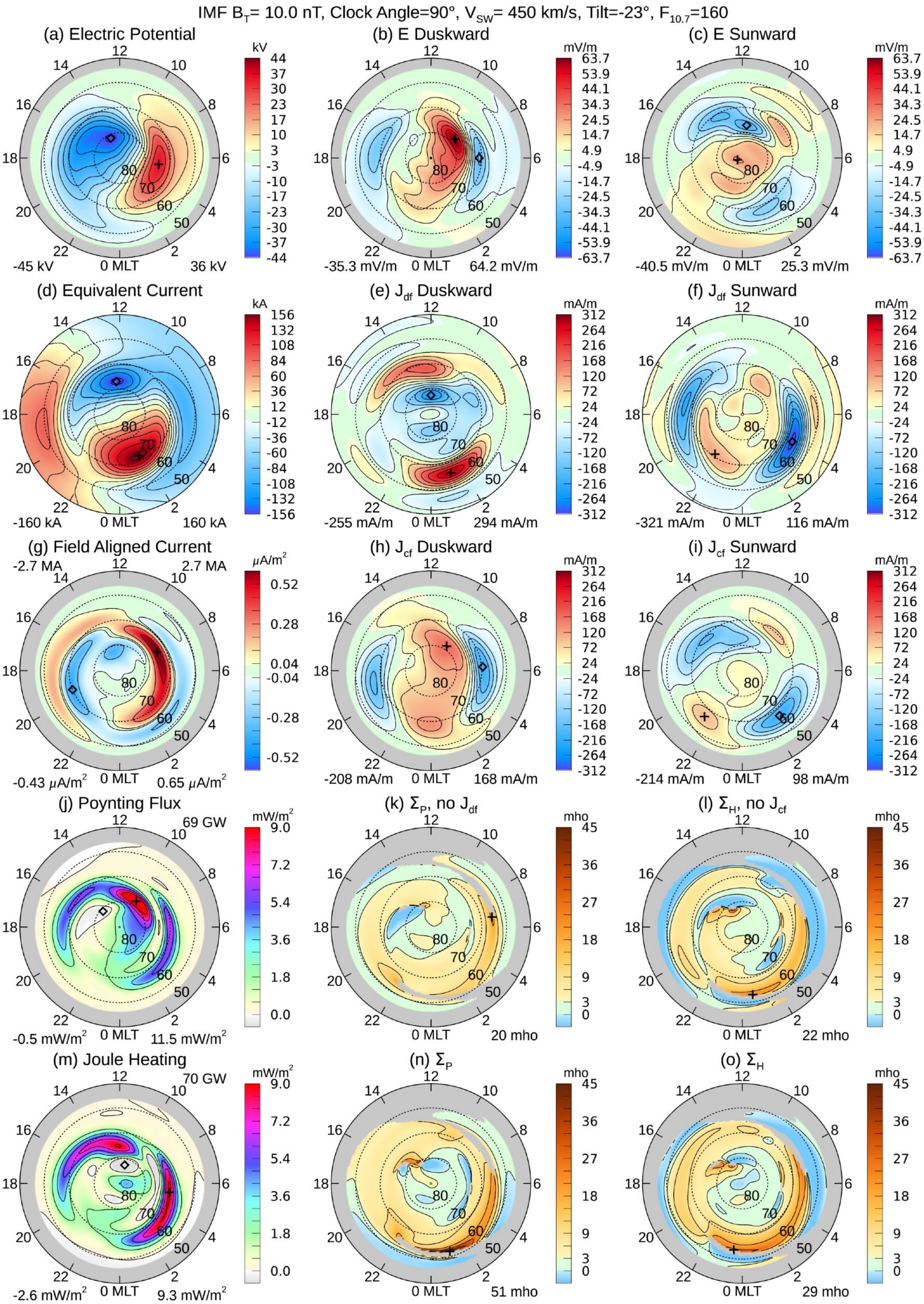

Figure S1. Conductivity input data and results, for IMF B_T magnitude 10 nT at 90° clock angle, and the dipole tilt angle is $-23°$.

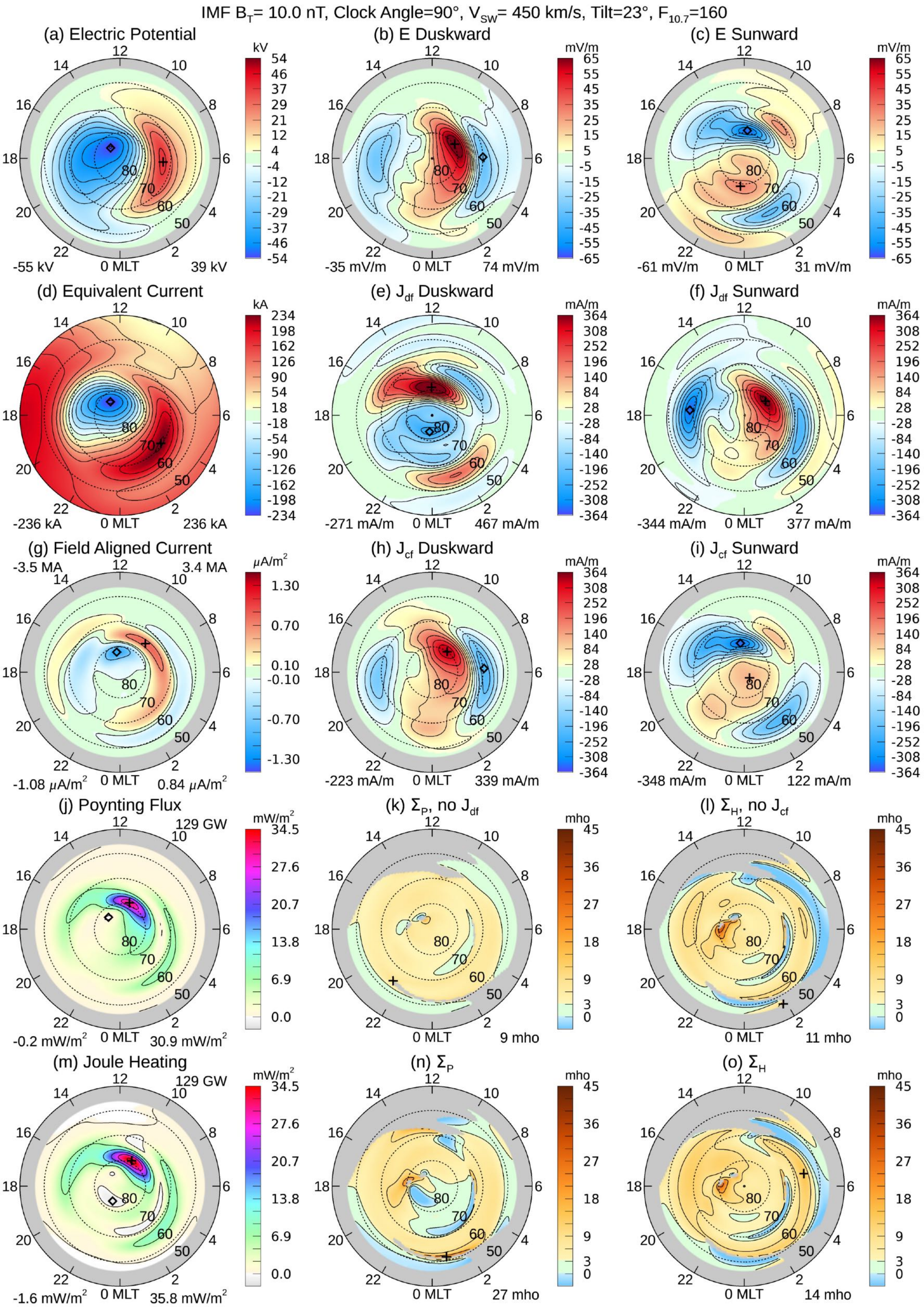

Figure S2. Conductivity input data and results, for IMF B_T magnitude 10 nT at 90° clock angle, and the dipole tilt angle is +23°.

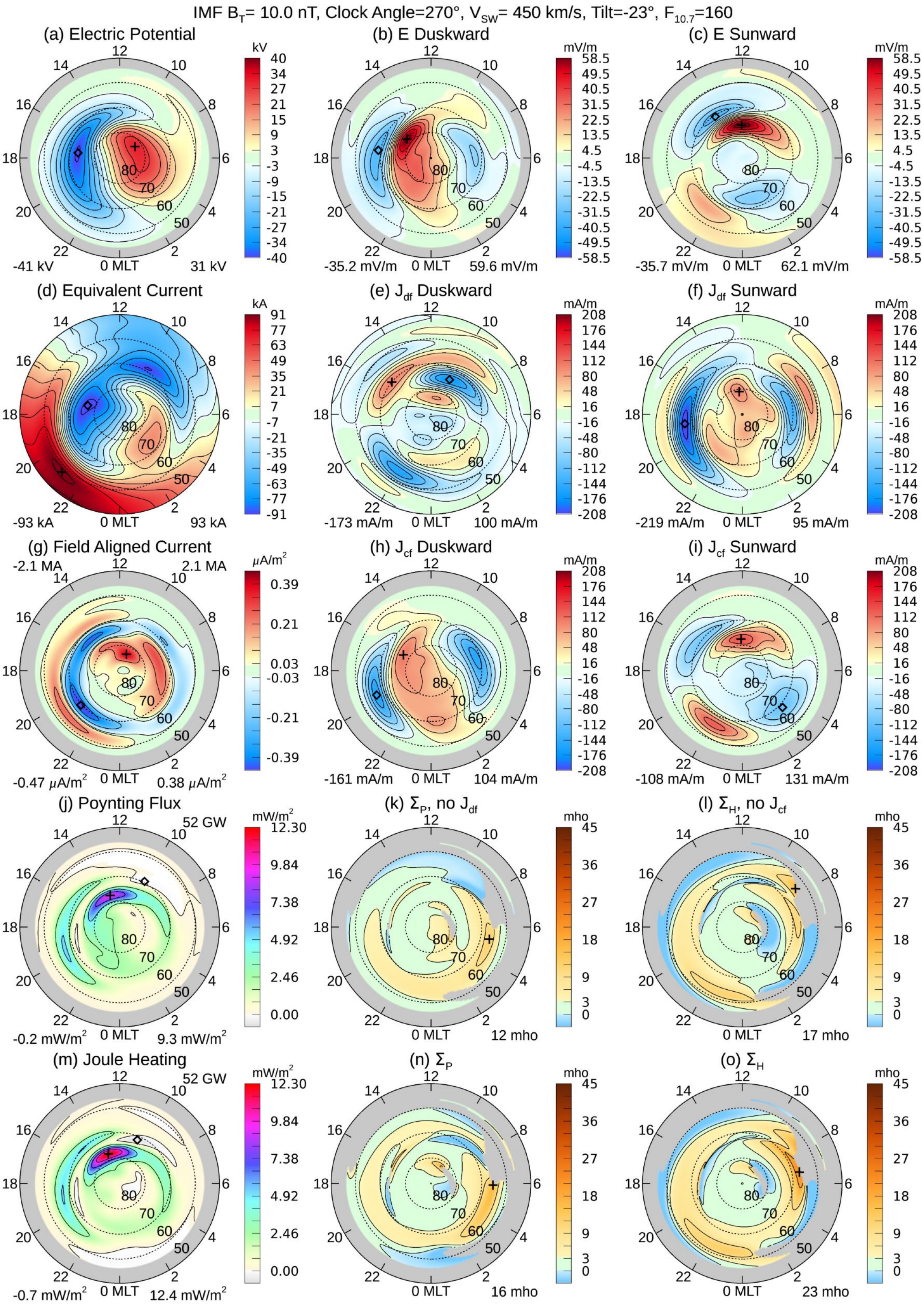

Figure S3. Conductivity input data and results, for IMF B_T magnitude 10 nT at 270° clock angle, and the dipole tilt angle is $-23°$.

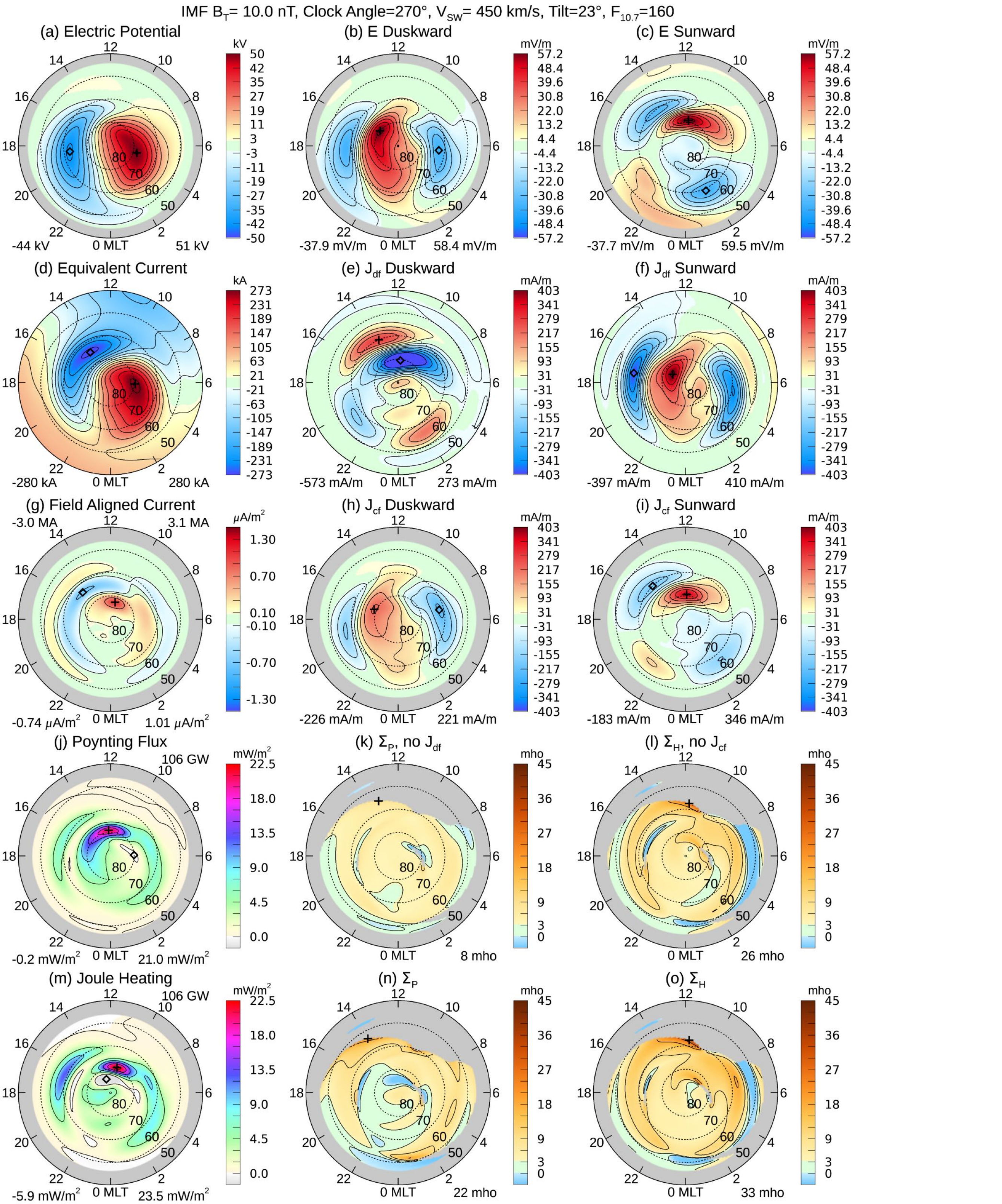

Figure S4. Conductivity input data and results, for IMF B_T magnitude 10 nT at 270° clock angle, and the dipole tilt angle is +23°.

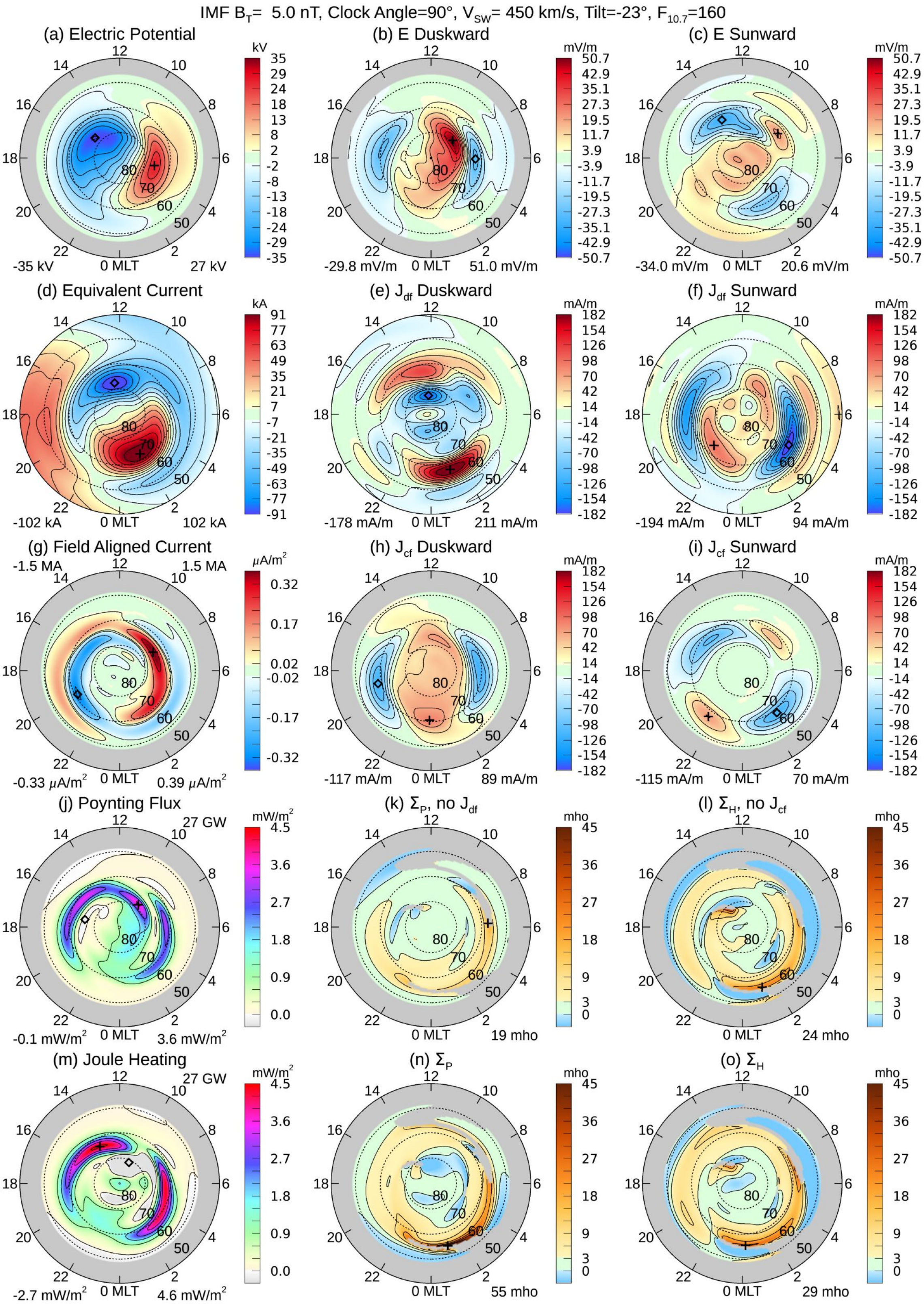

Figure S5. Conductivity input data and results, for IMF B_T magnitude 5 nT at 90° clock angle, and the dipole tilt angle is $-23°$.

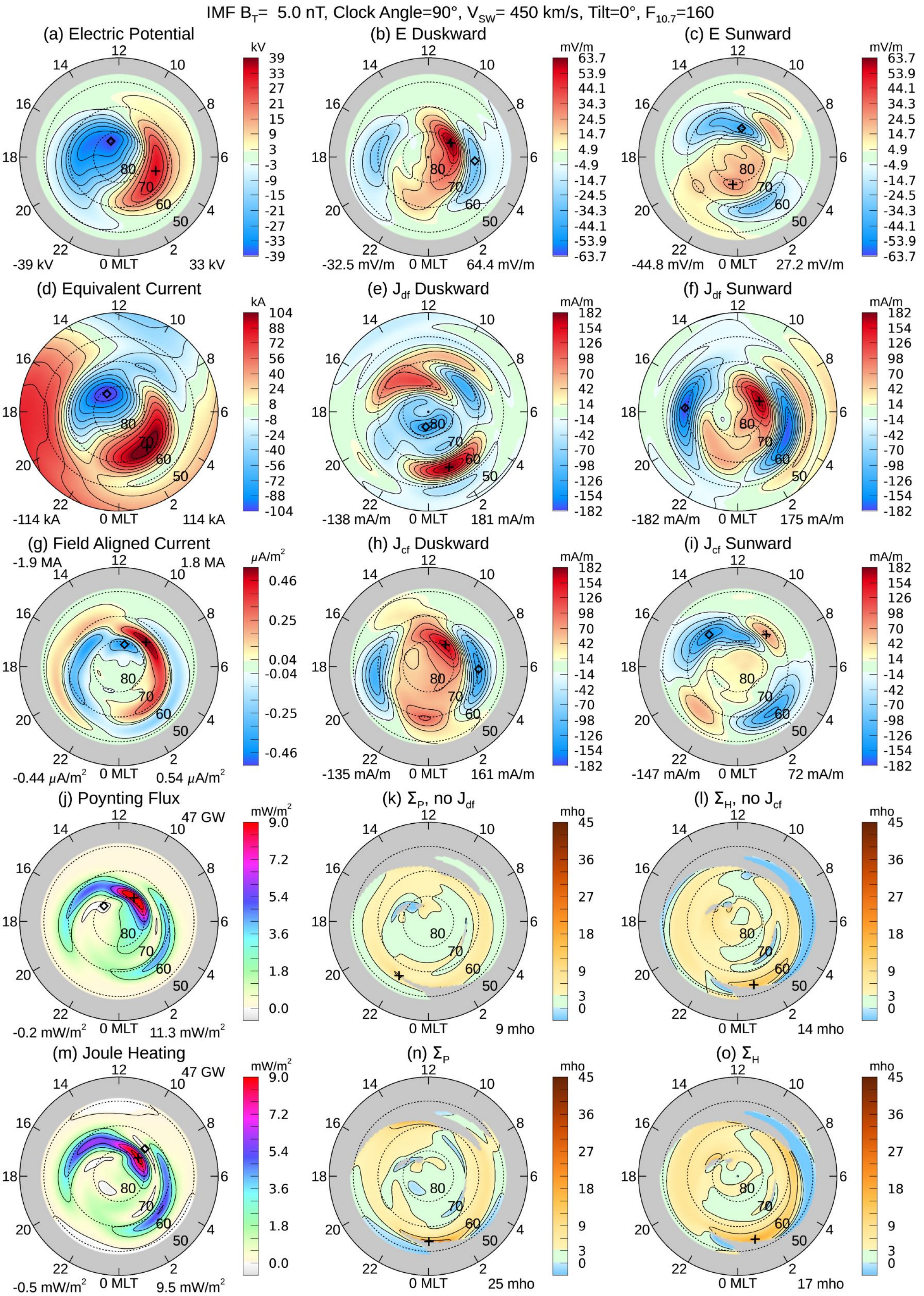

Figure S6. Conductivity input data and results, for IMF B_T magnitude 5 nT at 90° clock angle, and the dipole tilt angle is 0°.

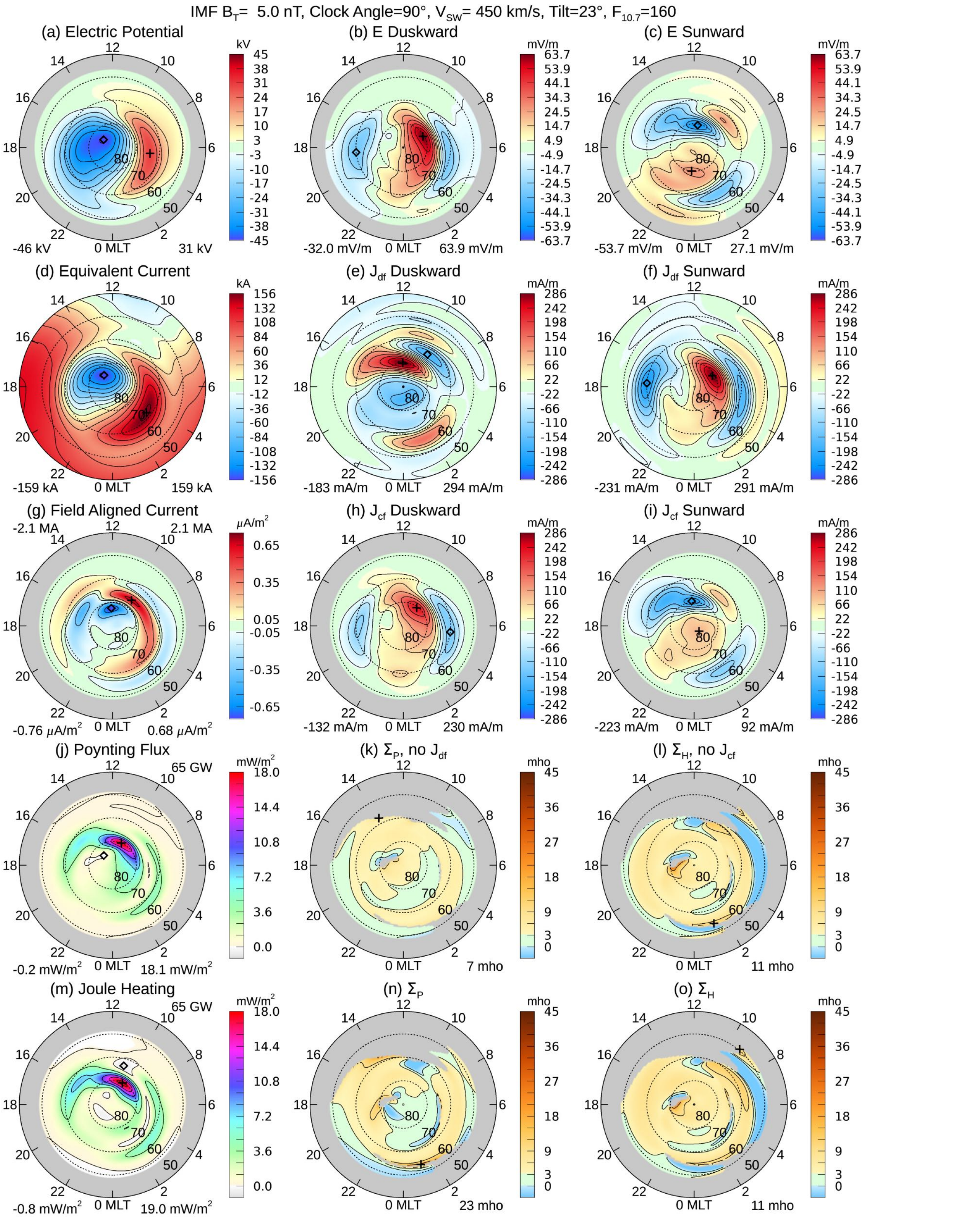

Figure S7. Conductivity input data and results, for IMF B_T magnitude 5 nT at 90° clock angle, and the dipole tilt angle is +23°.

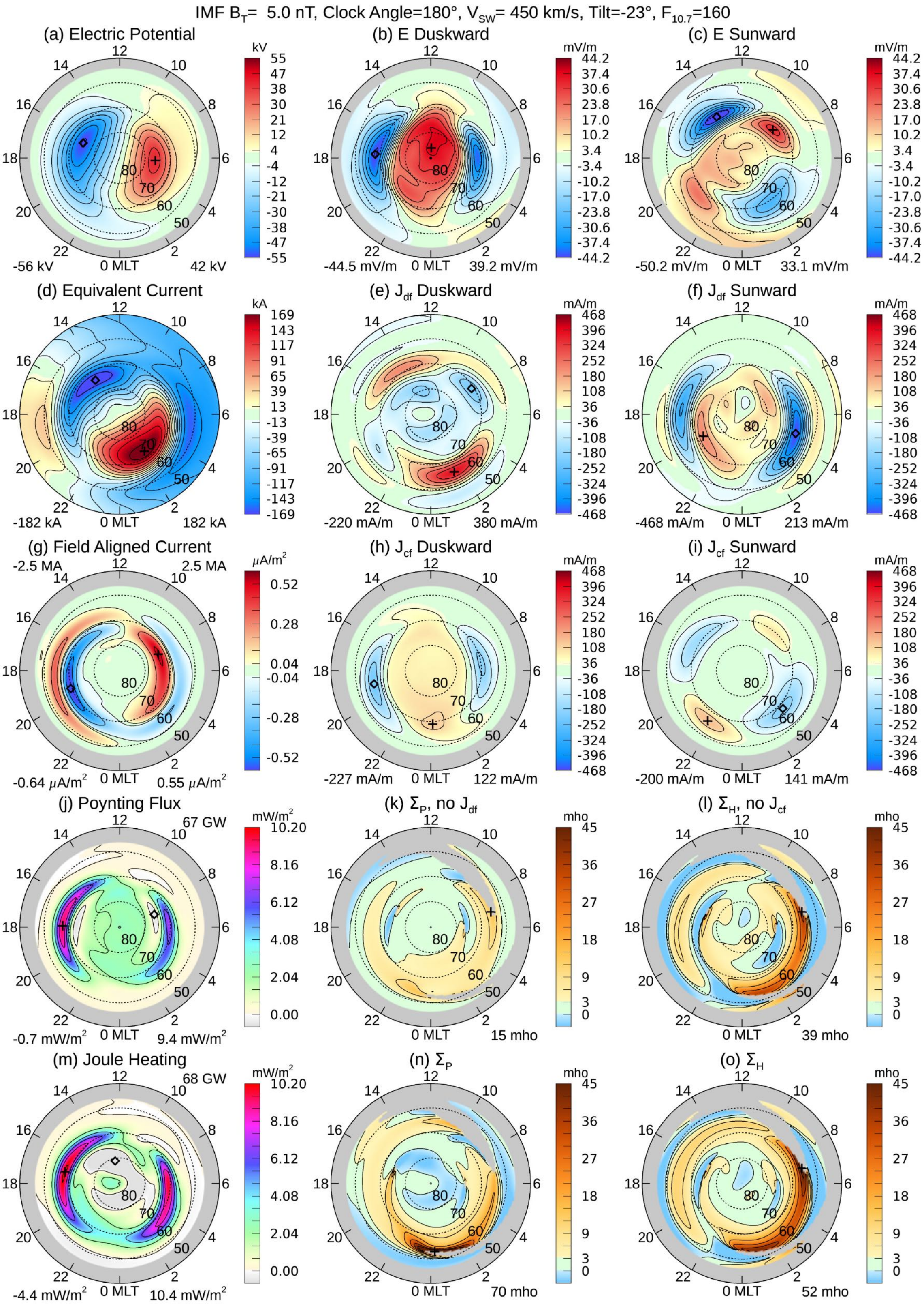

Figure S8. Conductivity input data and results, for IMF B_T magnitude 5 nT at 180° clock angle, and the dipole tilt angle is $-23°$.

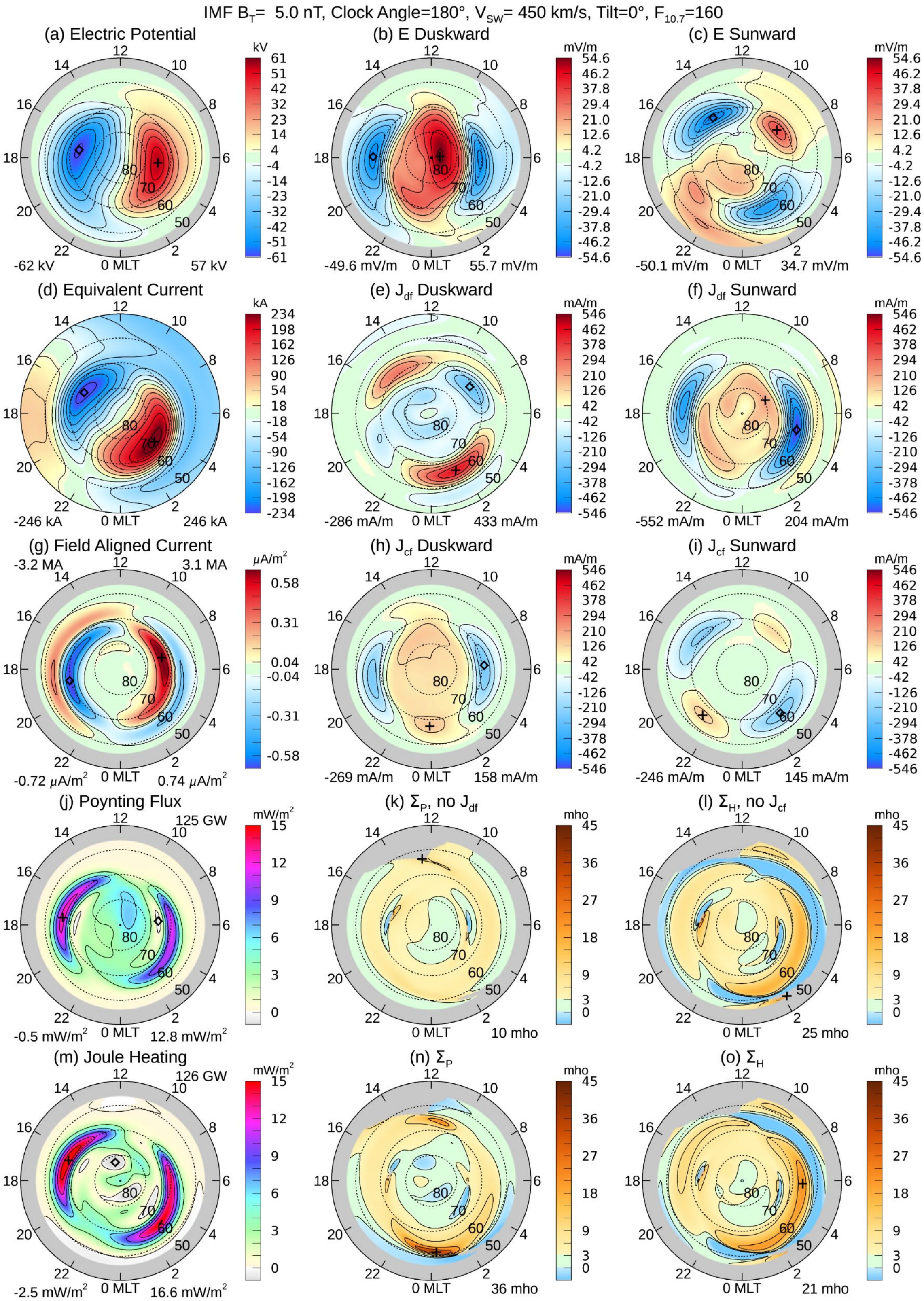

Figure S9. Conductivity input data and results, for IMF B_T magnitude 5 nT at 180° clock angle, and the dipole tilt angle is 0°.

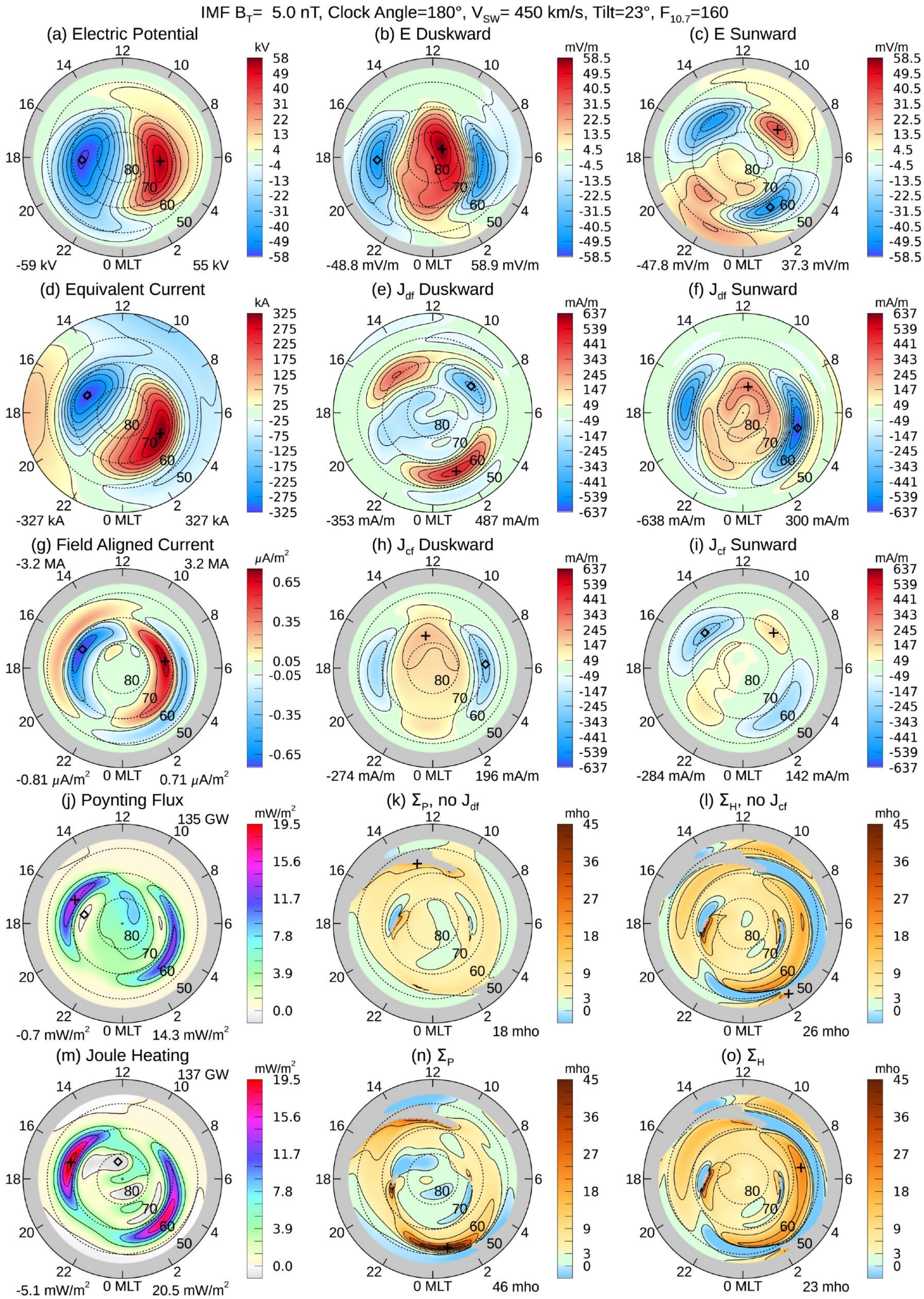

Figure S10. Conductivity input data and results, for IMF B_T magnitude 5 nT at 180° clock angle, and the dipole tilt angle is +23°.

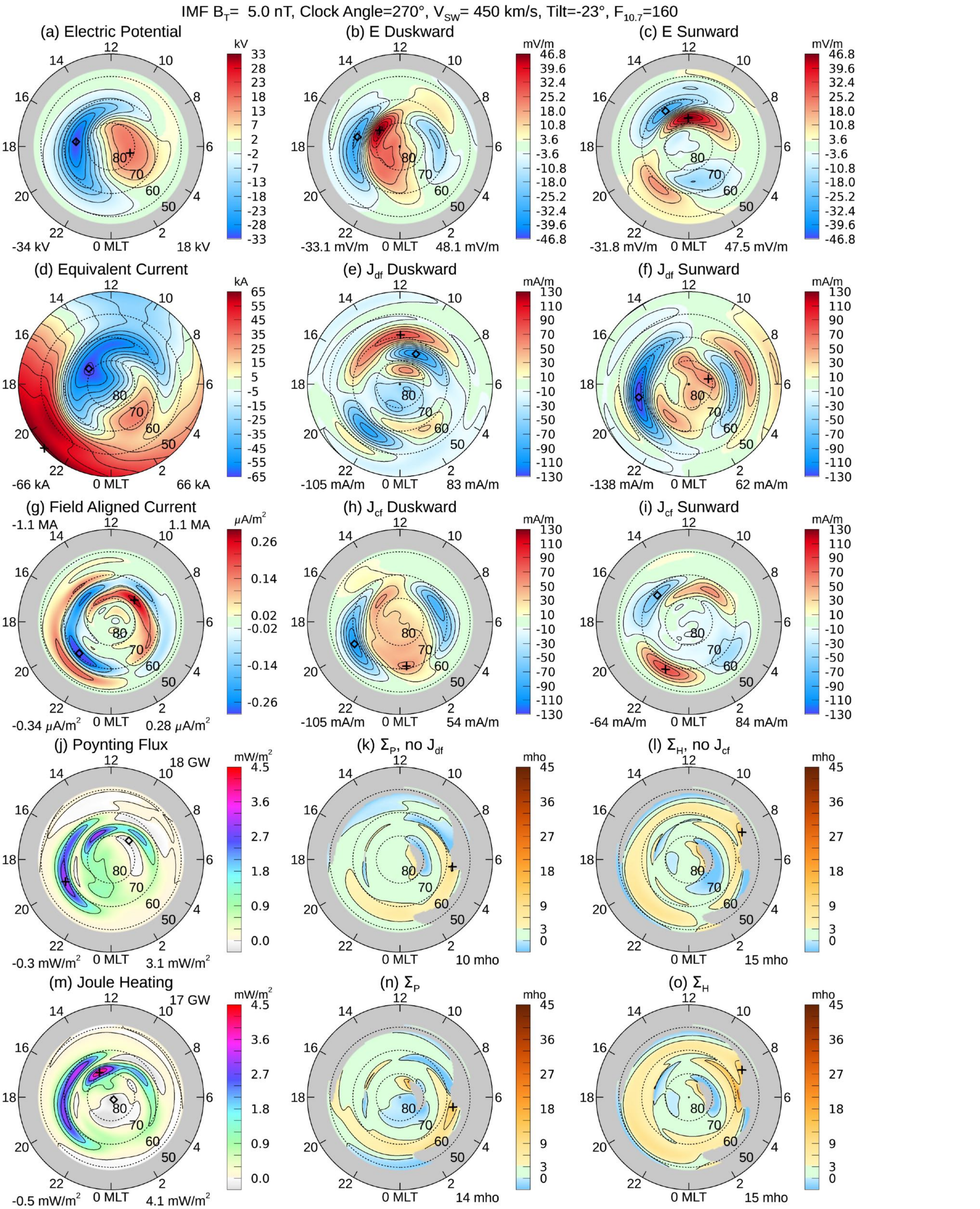

Figure S11. Conductivity input data and results, for IMF B_T magnitude 5 nT at 270° clock angle, and the dipole tilt angle is $-23°$.

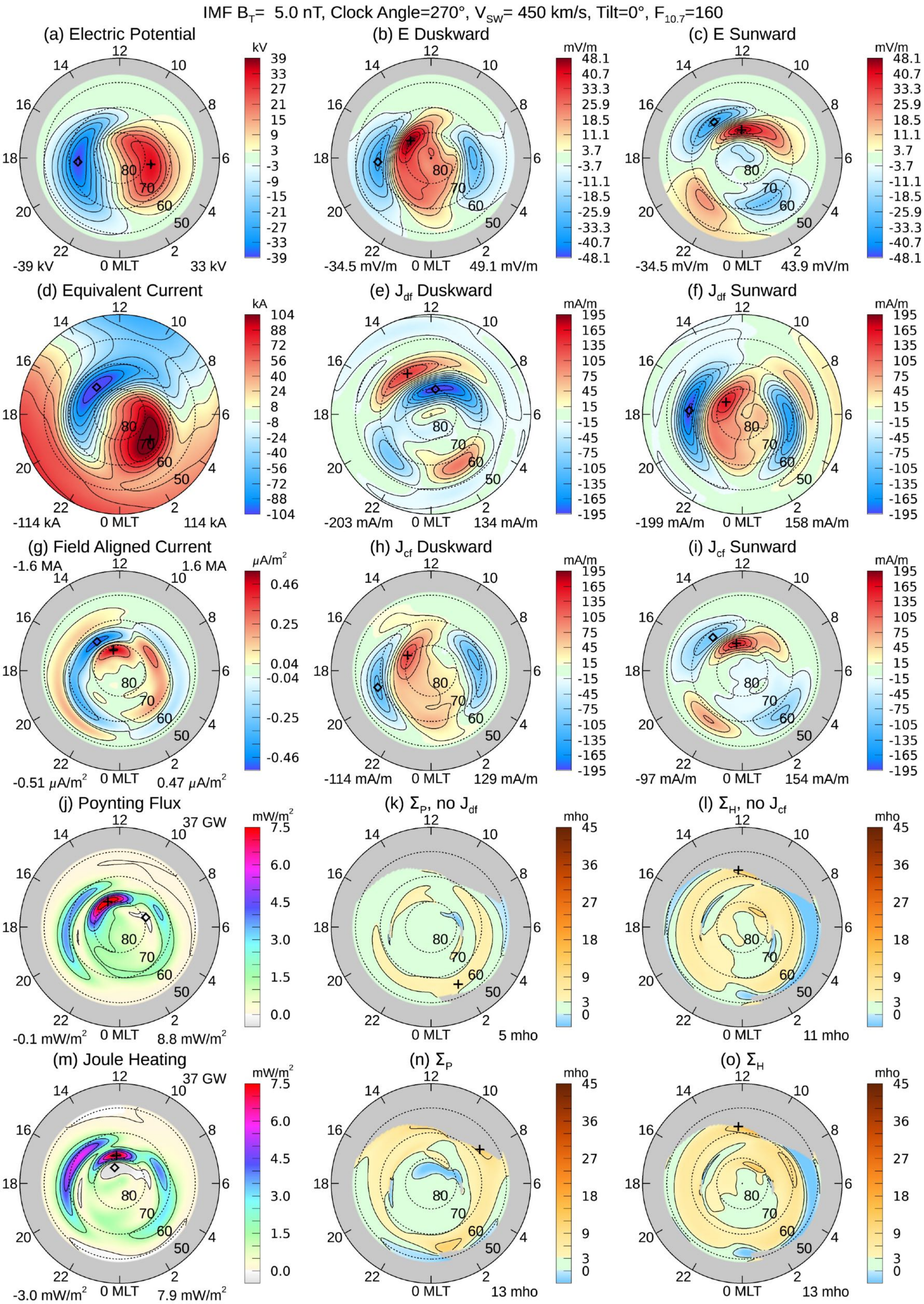

Figure S12. Conductivity input data and results, for IMF B_T magnitude 5 nT at 270° clock angle, and the dipole tilt angle is 0°.

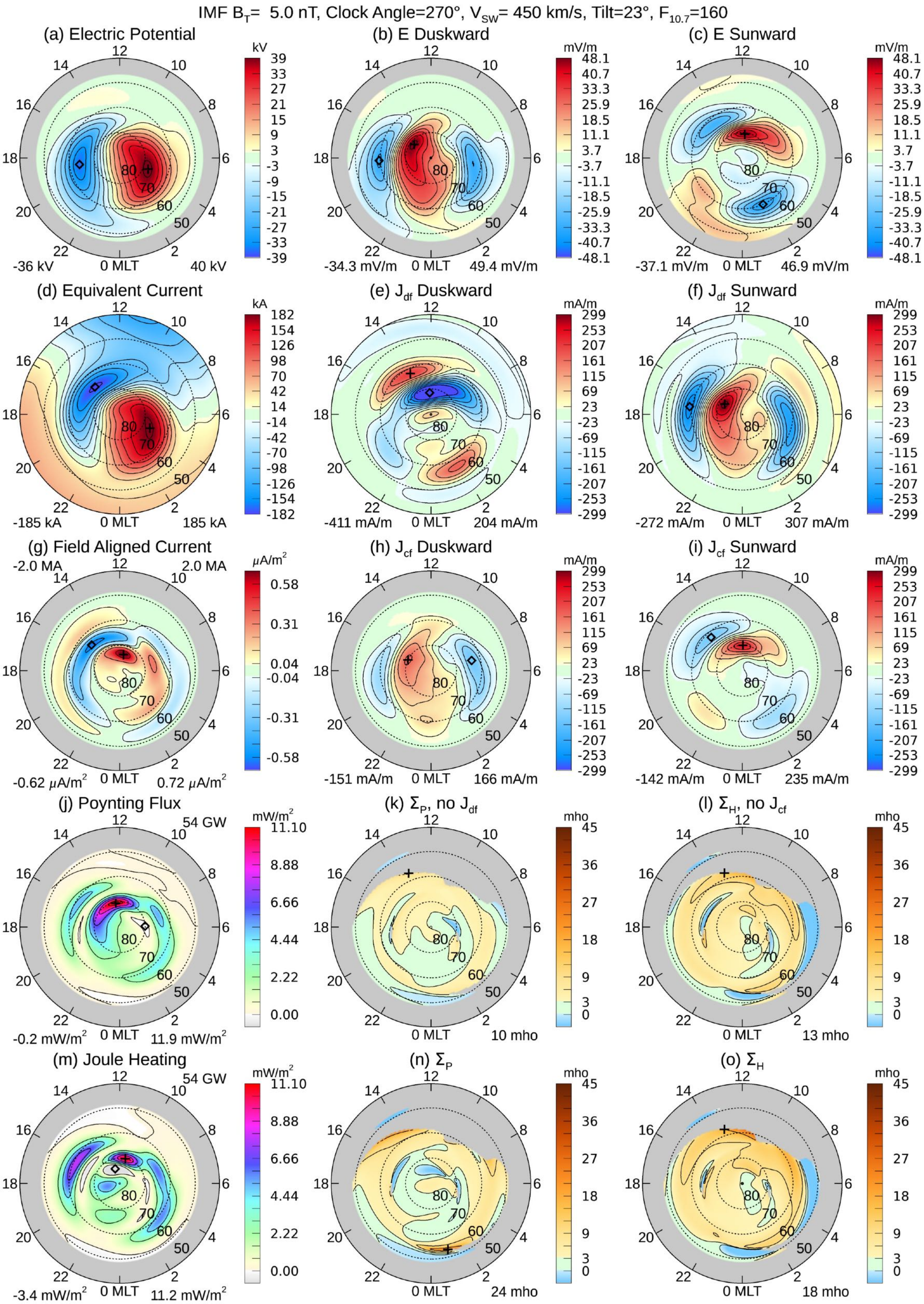

Figure S13. Conductivity input data and results, for IMF B_T magnitude 5 nT at 270° clock angle, and the dipole tilt angle is +23°.